Mutation-related magnetization-transfer, not axon density, drives white matter differences in premanifest Huntington's disease: Evidence from *in vivo* ultra-strong gradient MRI

Running title:

Mutation-related WM differences in HD

Chiara Casella[1,2], Maxime Chamberland[1,3], Pedro Luque Laguna[1], Greg D. Parker[1], Anne E. Rosser[4,5], Elizabeth Coulthard[6], Hugh Rickards[7,8], Samuel C. Berry[1], Derek K. Jones[1†], Claudia Metzler-Baddeley[1†]

[†]**These authors share senior authorship.**

Author affiliations:

1 Cardiff University Brain Research Imaging Centre (CUBRIC), School of Psychology, Cardiff University, Cardiff, CF 24 4HQ, UK.

2 Department of Perinatal Imaging and Health, School of Biomedical Engineering & Imaging Sciences, King's College London, 1st Floor South Wing, St Thomas' Hospital, London, SE1 7EH, UK.

3 Donders Institute for Brain, Cognition and Behavior, Radboud University, Nijmegen, The Netherlands.

4 Department of Neurology and Psychological Medicine, Hayden Ellis Building, Cardiff, CF24 4HQ, UK.

5 School of Biosciences, Cardiff University, Cardiff, CF10 3AX, UK.

6 Bristol Medical School, University of Bristol, Bristol, BS10 5NB, UK.

7 Birmingham and Solihull Mental Health NHS Foundation Trust, Birmingham, B1 3RB, UK.

8 Institute of Clinical Sciences, College of Medical and Dental Sciences, University of Birmingham, Edgbaston, Birmingham, B15 2TT, UK.

Correspondence to: Dr Chiara Casella
Full address: Department of Perinatal Imaging and Health, School of Biomedical Engineering & Imaging Sciences, King's College London, 1st Floor South Wing, St Thomas' Hospital, London, SE1 7EH, UK.
E-mail: chiara.casella@kcl.ac.uk

Funding and acknowledgements

The present research was funded by a Wellcome Trust PhD studentship to CC (ref: 204005/Z/16/Z); DKJ was supported by a New Investigator Award (to DKJ) from the Wellcome Trust (ref: 096646/Z/11/Z) and a Strategic Award from the Wellcome Trust (ref: 104943/Z/14/Z). We thank Dr Slawomir Kusmia and Dr Elena Kleban for their support with the project.

Abstract

White matter (WM) alterations have been observed in Huntington's disease (HD) but their role in the disease-pathophysiology remains unknown. We assessed WM changes in premanifest HD by exploiting ultra-strong-gradient magnetic resonance imaging (MRI). This allowed to separately quantify magnetization transfer ratio (MTR) and hindered and restricted diffusion-weighted signal fractions, and assess how they drove WM microstructure differences between patients and controls. We used tractometry to investigate region-specific alterations across callosal segments with well-characterized early- and late-myelinating axon populations, while brain-wise differences were explored with tract-based cluster analysis (TBCA). Behavioural measures were included to explore disease-associated brain-function relationships. We detected lower MTR in patients' callosal rostrum (tractometry: $p = 0.03$; TBCA: $p = 0.03$), but higher MTR in their splenium (tractometry: $p = 0.02$). Importantly, patients' mutation-size and MTR were positively correlated (all p-values < 0.01), indicating that MTR alterations may directly result from the mutation. Further, MTR was higher in younger, but lower in older patients relative to controls ($p = 0.003$), suggesting that MTR increases are detrimental later in the disease. Finally, patients showed higher restricted diffusion signal fraction (FR) from the Composite Hindered and Restricted Model of Diffusion (CHARMED) in the cortico-spinal tract ($p = 0.03$), which correlated positively with MTR in the posterior callosum ($p = 0.033$), potentially reflecting compensatory

mechanisms. In summary, this first comprehensive, ultra-strong gradient MRI study in HD provides novel evidence of mutation-driven MTR alterations at the premanifest disease stage which may reflect neurodevelopmental changes in iron, myelin or a combination of these.

Keywords: premanifest Huntington's disease; white matter microstructure; myelin; axon; MRI.

Key points:

i. The very latest-in ultra-strong magnetic field gradient technology was exploited to assess WM microstructure in premanifest HD patients with multi-modal quantitative MRI.
ii. Novel evidence of mutation-driven MTR alterations at the premanifest disease stage is provided
iii. This may reflect neurodevelopmental changes in iron, myelin or a combination of these.

Introduction

Huntington's disease (HD), a neurodegenerative disorder leading to devastating cognitive, psychiatric and motor symptoms, cannot currently be cured, and a research priority is to increase understanding of its pathogenesis. Subtle and progressive white matter (WM) alterations have been observed early in HD progression [1–7], but their aetiology and role remain unclear. Therefore, the present study aimed to disentangle the contribution of changes in axon microstructure *versus* changes in magnetization transfer as a proxy measure of myelin and/or iron, to WM pathology in premanifest HD. Crucially, we exploited the very latest-in ultra-strong magnetic field gradient technology [8,9] to achieve high-b-values per unit each time and increased precision in the estimates of hindered and restricted diffusion signal fractions. In turn, this afforded an enhanced differential attenuation of intra- and extra-axonal MRI signals, while maintaining sufficient signal-to-noise ratio (SNR), and thus allowed us to better tease apart the contribution of different sub-compartments of WM microstructure [10–12]. More specifically, we used multi-modal quantitative MRI to assess WM microstructure in premanifest patients relative to age and sex-matched healthy participants, and combined i. fractional anisotropy (FA), axial diffusivity (AD) and radial diffusivity (RD) from diffusion

tensor (DT)-MRI [13], with ii. The magnetization transfer ratio (MTR) from magnetization transfer imaging (MTI) as a proxy measure of myelin and iron differences, and iii. the restricted diffusion signal fraction (FR) from the Composite Hindered and Restricted Model of Diffusion (CHARMED) [14] as a proxy measure of changes in axon density [15]. Alterations in microstructural metrics were assessed using two analytical pipelines: i. a tractometry approach [16–18], in which the average value of a metric along a specific white matter bundle is derived, to assess tract-specific changes across the corpus callosum (CC), and ii. a whole-brain approach [19] to explore the pattern of abnormalities associated with the premanifest disease stage across all of the brain white matter.

The CC is the brain's largest WM tract and its fibres vary in size and age of myelination, with larger, early myelinating fibres occupying posterior, and smaller, later-myelinating fibres anterior callosal regions [20]. Thus, characterising WM microstructure across this tract affords insights into the impact of HD on regions with different axonal populations, and may aid in elucidating disease-related pathological processes in the context of the Demyelination Hypothesis [21]. This hypothesis proposes that mutant huntingtin (*mHTT)* leads to premature myelin breakdown, and has been given support by several animal studies demonstrating alterations in myelin-associated biological processes at the cellular and molecular level in the HD brain [22–28]. For example, electron microscopy investigations have reported thinner myelin sheaths in transgenic BACHD rats and in the HdhQ250 knock-in mouse model [22,24]. Such alterations in myelin sheaths are paralleled by the reduced expression of myelin-related genes such as myelin basic protein (*MBP*) and myelin oligodendrocyte glycoprotein (*MOG*) in transgenic R6/2 and HdhQ250 knock-in mice [22,26,29]. Moreover, these findings are accompanied by evidence of oligodendrocytes alterations provided by both animal and human post-mortem studies [22,23,25,27,30–32] . Specifically, although increased numbers of oligodendrocytes have been observed, evidence suggests that their dysfunctionality may lead to unsuccessful myelination, or that the observed increased levels of oligodendrocytes may be helpful at first but may eventually lead to increased iron toxicity. Both explanations fit within the demyelination hypothesis as they implicate an increasingly unsuccessful compensation for the disease-related myelin loss. For a critical review of human and animal studies lending support to the Demyelination Hypothesis see Casella et al. [7].

The Demyelination Hypothesis proposes that myelin impairment begins from early-myelinating caudate and putamen striatum structures and then spreads in a bilateral and symmetric pattern to other early-myelinating regions. Thus, in the context of the present

study, the Demyelination Hypothesis would predict more dominant microstructural changes in posterior relative to anterior callosal subregions, as the former myelinate earlier. Following evidence that WM volume loss in HD extends beyond the CC [2,33–39], and the concept of compensatory networks in response to neurodegeneration [40], we supplemented the tractometry analysis with a novel exploratory, whole-brain analysis, called Tract-Based Cluster Analysis (TBCA)[19] to assess brain-wise group microstructural differences. TBCA uses the rich anatomical information from whole-brain tractography reconstructions to inform the cluster-level inference analysis of voxel-based images, and provides the anatomical specificity required to disentangle distinct clusters belonging to different anatomical tracts [19]. Finally, the evidence of cognitive and behavioral impairments in premanifest patients [2,39,41] across attention, working memory, processing speed, psychomotor functions, episodic memory, emotion processing, sensory-perceptual functions, and executive functions [2,42–47], and their significant impact on everyday functional decline [48–50], stress the importance of understanding how these symptoms may relate to pathological neural changes, such as alterations in WM microstructure. For this purpose, we derived a composite cognitive score using principal component analysis (PCA) to capture variability in patients' cognitive performance and then used it for the analysis of correlations between differences in cognition and WM microstructure.

Materials and methods

Participants

Twenty-five individuals with premanifest HD and 25 age- and sex-matched healthy controls were recruited, with ethical approval from the local National Health Service (NHS) Research Ethics Committee (Wales REC 5 18/WA/0172) and by the Cardiff University School of Psychology Ethics Committee. All participants provided written informed consent prior to taking part in the study.

Patients were recruited from the Cardiff HD Research and Management clinic, Bristol Brain Centre at Southmead Hospital, and the HD clinic at the Birmingham and Solihull NHS Trust. Healthy controls were recruited from Cardiff University and the School of Psychology community panel. Participants were recruited if eligible for MRI scanning. Control

155 participants were excluded if they had a history of neurological or psychiatric conditions, and
156 patients if they had a history of any other neurological condition.
157 Twenty-two of the HD patients had pen-and-paper cognitive task data available from their
158 most recent participation in the ENROLL-HD study (NCT01574053, https://enroll-hd.org).
159 The progression of symptoms in ENROLL-HD participants is monitored longitudinally, and
160 one of the optional components within the study is the giving of permission by participants
161 for their coded data to be accessed by researchers in the field. As such, a full clinical dataset
162 including full medical and medication history is available for each research participant and
163 some of these data were used in this study.
164 One control subject was excluded from the tractometry analysis because of poor callosal
165 segmentation. Therefore, data from 25 patients and 24 healthy controls were used for callosal
166 tractometry analysis. As the callosal segmentation did not impact TBCA, a sample of 25
167 patients and 25 controls was analysed. Table 1 provides a summary of participants'
168 demographic and clinical background information. Performance in the Montreal Cognitive
169 Assessment (MoCA) [51] and in the Test of Premorbid Functioning - UK Version (TOPF-UK)
170 [52] is reported for patients and controls. The Unified Huntington Disease Rating Scale
171 (UHDRS) total motor score (TMS), total functional capacity (TFC), diagnostic confidence
172 level (DCL) and CAG repeat size obtained from the ENROLL-HD database are also reported
173 for patients.
174

175 # Data acquisition

176 ## Assessment of disease-related brain-function relationships

177 A composite cognitive score was computed by combining cognitive data available for
178 patients on the ENROLL-HD database (providing these had been obtained within a 3-month
179 time window from their participation in the present study), with data acquired during the
180 study. This was done in order to reduce patient burden associated with study participation.
181 Table 2 provides details on the administered tests, the cognitive domains they assess, and the
182 outcome variables measured.
183 Briefly, data from the ENROLL-HD database concerned performance in the Phonetic Verbal
184 Fluency Test, the Categorical Verbal Fluency Test, the Symbol Digit Modality Test, the

185 Stroop Colour Reading and Word Reading Test, the Stroop Interference Test and the Trail
186 Making Test [53–55]– please see http://www.enroll-hd.org for the detailed study protocol.
187 On the other hand, performance in the N-back Task [56], the Forward Digit Span Test adapted
188 from the Wechsler Adult Intelligence Scale-Revised (WAIS-R) [57], the Visual Patterns Test [58]
189 and the Speeded Finger Tapping Task [59] was assessed as part of the present study. Cognitive
190 testing was performed prior to MRI scanning and lasted approximately 60 minutes. Tasks
191 were administered either as paper and pencil tests or by using a computerized version
192 provided by the Psychology Experiment Building Language (PEBL) test battery [60].
193 As each task yields several outcome variables, the following strategy was employed: (1) for
194 standardized clinical tests, metrics known to have the best sensitivity and measurement
195 characteristic were selected, e.g. correctly-generated responses instead of error scores [61]; (2)
196 for tests with multiple conceptually distinct outcome measures, variables that represented
197 each component were included, e.g., for the N-back Task, the number of correct responses
198 from the 1-back and the 2-back condition; and (3) where necessary, variables were excluded
199 from the assessment, e.g. when these presented lots of missing cases. This approach led to 13
200 cognitive outcome measures (Table 2).
201

202 ## MRI data acquisition

203 MRI data were acquired on a 3 Tesla Siemens Connectom system with ultra-strong (300
204 mT/m) gradients. Each MRI session lasted 1 hour, and comprised: a T_1-weighted MPRAGE;
205 a multi-shell dMRI acquisition [δ/Δ: 7/24 ms; b-values: 0 (14 volumes, interleaved), 500 (30
206 directions), 1200 (30 directions), 2400 (60 directions), 4000 (60 directions), and 6000 (60
207 directions) s/mm^2 [63]. Data were acquired in an anterior-posterior phase-encoding direction,
208 with one additional posterior-to-anterior volume]; and a magnetization transfer acquisition
209 [turbo factor: 4; radial reordering; non-selective excitation; MT contrast was achieved by the
210 application of a 15.36 ms radio-frequency saturation pulse, with an equivalent flip angle of
211 333° applied at a frequency of 1.2 kHz below the water resonance. Two identical sets of
212 images with different contrasts (one acquired with and one acquired without MT saturation
213 pulses) were obtained]. Table 3 provides more details on the acquisition parameters.
214

Image processing

All images were skull-stripped in native space using FSL BET [64].

Diffusion data: FA, RD, AD, MD and FR maps

Pre-processing of diffusion data was carried out using FMRIB Sofware Library (FSL) [64], MRtrix3 [65], and Advanced Normalization Tools (ANTs) [66]. These steps included: denoising [67], slice-wise outlier detection (SOLID) [68], and correction for drift [69]; motion, eddy, and susceptibility-induced distortions [70,71]; Gibbs ringing [72]; bias field [73]; and gradient non-linearities [74,75].

Diffusion tensors were estimated using linearly-weighted least squares regression (for $b < 1200$ s/mm^2 data) providing the following quantitative scalar measures: FA, AD and RD. The diffusion tensor was fitted to data between $b = 500$ s/mm^2 and $b = 1200$ s/mm^2 in order to reduce cerebrospinal fluid based partial volume artefacts in the DTI metrics. The CHARMED data were corrected for motion and distortion artefacts [76], before computing FR maps [14] using in-house software coded in MATLAB (The MathWorks, Natick, MA).

Magnetization transfer: MTR maps

MT- and non-MT-weighted images were corrected for Gibbs ringing [72]. ANTS [66] was first used to nonlinearly register the MPRAGE images to the $b = 0$ s/mm^2 images. Then MT- and non-MT weighted images were linearly warped to the registered MPRAGE images using an affine (12 degrees of freedom) technique based on mutual information, with the FMRIB's Linear Image Registration Tool (FLIRT)[77]. All registrations were visually inspected for accuracy. Finally, MTR maps were calculated according to: $MTR = [(S^0 - S^{MT})/S^0] \times 100$, whereby S^0 represents the signal without the off-resonance pulse and S^{MT} represents the signal with the off-resonance pulse.

Tractography of the CC

Automated WM tract segmentation of the CC was performed using TractSeg [78] and multi-shell constrained spherical deconvolution (MSMT-CSD) [79]. Specifically, seven portions of the CC were delineated [1=rostrum, 2=genu, 3=rostral body, 4=anterior midbody,

5=posterior midbody; 6=isthmus, 7=splenium] (Fig. 1). For each segment, 2000 streamlines were generated.

Statistical analysis

Analyses were performed in RStudio [80], MATLAB (The MathWorks, Natick, MA), SPSS [81], the PROCESS computational tool for mediation analysis [82], FSL [64], and the Statistical Non-Parametric Mapping (SnPM) software [83]. Outliers were first identified by examining box-and-whisker plots for each dependent variable, for controls and patients separately. Outliers that were ± 3 standard deviations from the mean were removed.

Assessment of disease-related brain-function relationships

PCA of the cognitive data was performed on the slopes of the patient data to best capture heterogeneity within this population. Only the first principal component (PC) was extracted, to increase experimental power and reduce the number of multiple comparisons [84].
First, the Bartlett's test of sphericity and the Kaiser-Meyer-Olkin (KMO) test were used to confirm that the data were suited for PCA [KMO = 0.54, $\chi 2$ (78) = 156.5, p <0 .001]. The PCA was run using centred, standardized versions of the patients' cognitive outcome scores. Orthogonal Varimax rotation was used to maximize the factor loadings. Regression values from each component were used as composite cognitive scores for each patient.

Tractometry of the CC

Microstructure differences were assessed in the seven callosal segments. By taking each quantitative metric map, samples of each metric were obtained at each vertex of the reconstructed segments, and segment-specific medians were derived for FA, AD, RD, FR and MTR in MRtrix3 [65]. Next, the overall mean was calculated, so that each dataset comprised $m = 5$ MRI-derived measures, mapped along s = 7 callosal segments.

Reduction of MRI data dimensionality with PCA

PCA was also employed to reduce the complexity of the callosal microstructure data [85]. Centred, standardized versions of MRI measures on both groups combined were used [86].

Specifically, the PCA was calculated for FA, FR, RD, AD and MTR, after checking that the data was suited for this analysis [KMO = 0.65, χ^2 (6) = 1077.231, $p < 0.001$]. PCA was applied to the concatenated set of segments across subjects [87,88]. The number of principal components was extracted based on: 1) their interpretability [89]; 2) the Kaiser criterion of including all components with an eigenvalue greater than 1. Regression values from each component for each participant were used in the following analyses.

Investigation of group differences in callosal microstructure

To assess group differences in callosal microstructure, analyses of covariance (ANCOVAs) were run on the extracted regression values from each component for each participant. Group and segment were used as independent variables because of a particular interest in understanding the interaction between group effects on different callosal segments. The correlation of microstructure outcome measures across patients and controls, with age, ICV and TOPF-UK FSIQ was tested to decide if these variables should be included as covariates in the analysis. Pearson's correlation coefficients greater than 0.3 were treated as indicative of a moderate relationship. For every ANCOVA, analysis assumptions were first tested.

Assessment of disease-related brain-function relationships

Spearman correlations were run in the patient group for:

i. The extracted regression values from each significant component for each participant, and their respective composite cognitive scores;
ii. The extracted regression values from each significant component for each participant, and their respective CAG repeat length;
iii. The extracted regression values from each significant component for each participant, and their respective disease burden score (DBS), calculated as follows: DBS = age × (CAG-35.5).

Within each group of correlations, multiple comparison correction was carried out with Bonferroni with a family-wise alpha level of 5% (two-tailed). Whenever a significant association was detected, this was further explored with partial correlations, partialling out ICV and DBS. The latter was done to assess associations independently of disease progression.

TBCA assessment of brain-wise group differences in WM microstructure

TBCA [19] was applied to assess group differences in FA, RD, AD, FR and MTR. This method is based on the novel concept of a 'hypervoxel', which extends standard 3D voxels with extra dimensions to encode geometrical and topological information about the streamlines that intersect each voxel.

All images were first non-linearly normalised to the FMRIB58_FA template (1 × 1 × 1 mm isotropic) using the tbss_2_reg script [90]. Next, statistical maps were produced based on the voxel-level analysis of the data by using a non-parametric approach based on a permutation test strategy [91]. The statistical maps were then thresholded at $p = 0.01$, and the suprathreshold voxel-level statistic results were projected onto an hypervoxel template built on whole-brain tractography data from 20 healthy subjects. Two hypervoxels were defined as belonging to the same cluster if they were either adjacent or connected within the hypervoxel template (i.e. if they shared a common streamline) [19]. Finally, the mass of each cluster [92] was computed and their corresponding statistical significance calculated based on the same permutation tests used for the voxel-level inference. Explanatory variables (EVs) in the permutation tests included age and gender and the effect of group was explored whilst regressing the other EVs. Clusters with a family-wise error (FWE)-corrected [83] p-value below 0.05 were considered statistically significant. A schematic representation of the TBCA pipeline can be found in Fig. 2.

Whenever significant clusters were detected for a specific metric, these were extracted, summed and binarized to form an ROI mask. The mask was then projected onto each map in MNI space. The mean value for that metric was calculated in the ROI with FSL [64], and used to run Spearman correlations between the WM metrics showing significant clusters. Multiple comparison correction was carried out with the Bonferroni correction with a family-wise alpha level of 5% (two-tailed).

Results

Composite cognitive score in the patient sample

As shown in Fig. 3, the first principal component (PC) accounted for 38.7% of the total variance in the cognitive data. Component loadings of >= 0.5 were considered as significant [93]. Thus, this component reflected general executive functioning with loadings on distractor

suppression (Stroop task), attention switching (Trail Making), updating (N-back), category fluency and motor speed.

Reduction of MRI data dimensionality with PCA

Over 80% of the variability in the microstructure data was accounted for by the first two principal components (PC1, 58.1%, $\lambda = 2.90$; PC2, 22.6%, $\lambda = 1.13$). As shown in Fig. 4, the first PC loaded positively on FA, FR, and AD, and negatively on RD, measuring restriction or hindrance perpendicular to the main axis of the bundle, and was therefore summarized as "axon density" component. The second component loaded mostly on MTR and was thus summarized as "magnetization transfer" component.

Premanifest patients present alterations in callosal MTR but not axon density

Assessment of group differences in axon density

Age was negatively associated with axon density scores ($r = -0.301$, $p < 0.001$), and included in the final model assessing the effect of group and segment on axon density scores, with age as covariate.

The effect of group was not significant [$F(1, 312) = 1.677$, $p = 0.196$], however a main effect of segment was detected [$F(6, 312) = 84.671$, $p < 0.001$] (Fig. 4), together with a main effect of age [$F(1, 312) = 34.116$, $p < 0.001$] (Fig. 4). The Group × Segment interaction was not significant [$F(6, 312) = 0.531$, $p = 0.784$]. Overall, age was negatively associated with scores on this component; additionally, microstructure in the posterior segments of the CC was associated with higher axon density scores, compared to anterior ones [adjusted means: CC1 = -0.270; CC2 = -0.822; CC3 = -0.546; CC4 = -0.001; CC5 = -0.144; CC6 = 0.083; CC7 = 1.753].

Assessment of group differences in the magnetization transfer component

Age and ICV were correlated with scores on the magnetization transfer component (age: $r = -0.301$, $p < 0.001$; ICV: $r = -0.332$, $p < 0.001$), thus the final model assessed the main effects of group and segment, and age-by-group and a group-by-segment interactions, with age as covariate.

There were no main effects of group [$F(1, 312) = 2.353$, $p = 0.126$] or ICV [$F(1, 312) = 1.875$, $p = 0.172$]. However, significant main effects of age [$F(1,312) = 45.07$, $p < 0.001$] and segment [$F(1, 312) = 19.899$, $p < 0.001$] were detected. Overall, scores on this component were lower in segment 7 of the CC and in older participants (Fig. 4).

Crucially, a significant interaction was detected between segment and group [$F(6, 312) = 2.238$, $p = 0.040$], indicating that the effect of group was different for different callosal segments. Therefore, slopes of the effect of group on PC2 for each segment, while controlling for the effect of age, were investigated with a simple moderation analysis using the PROCESS toolbox for SPSS [82], to better understand this interaction.

This analysis revealed that patients presented significantly higher scores on the magnetization transfer component compared to controls in segment 1 ($p = 0.016$), and significantly lower scores in segment 7 ($p = 0.0343$). Overall, scores on this component for the patient group were higher than controls in the more anterior portions of the CC but lower in the posterior portions (segment1: $\beta = 0.56$, $t = 2.41$, $p = 0.016$; segment 2: $\beta = 0.25$, $t = 1.08$, $p = 0.27$; segment 3: $\beta = 0.014$, $t = 0.06$, $p = 0.95$; segment 4: $\beta = 0.2098$, $t = 0.90$, $p = 0.36$; segment 5: $\beta = 0.44$, $t = 1.89$, $p = 0.058$; segment 6: $\beta = -0.028$, $t = -0.12$, $p = 0.899$; $\beta = -0.5$, $t = -2.12$, $p = 0.034$) (Fig. 5).

As a post-hoc, exploratory analysis, the impact of partial volume artifacts on magnetization transfer differences between patients and controls was assessed. The fractional volume of free water in each voxel was estimated from the diffusion data to produce a free-water signal fraction (FWF) map. The overall mean FWF was then calculated, as described above for the other metrics assessed. Finally, an ANCOVA was run to assess group differences in magnetization transfer across the different segments, controlling for FWF. Specifically, the main effects of group and segment and their interaction effect were examined, with age, ICV and FWF as covariates. Age-by-group and group-by-FWF interactions were included in the model because of violation of the homogeneity of regression slopes assumption.

Consistent with the main analysis, a significant main effect of age [$F(1, 300) = 56.08$, $p < 0.001$] and segment [$F(1, 300) = 22.89$, $p < 0.001$] and a significant interaction effect between segment and group [$F(1,300) = 3.2$, $p = 0.005$] were detected. The interaction between group and age [$F(1, 300) = 8.736$, $p = 0.003$] was now significant, indicating that while scores on this component are lower than age-matched controls in older patients, the opposite was true for younger patients. Finally, a significant main effect of group [$F(1, 300)$

400 = 13.042, $p < 0.001$], and FWF [$F(1, 300) = 13.32$, $p < 0.001$], and a significant interaction
401 effect between group and FWF [$F(1, 300) = 19.262$, $p < 0.001$], were detected.
402
403
404 **Magnetization transfer is associated with CAG repeat length but**
405 **not with cognitive performance or disease burden**
406
407 Spearman correlation coefficients and associated p-values for the correlations of
408 magnetization transfer with composite cognitive scores, CAG repeat length and DBS are
409 reported in Table 4. Trends for positive associations were detected between composite
410 cognitive scores and magnetization transfer in all segments, except for segment 7. However,
411 these associations were no longer significant after multiple comparison correction.
412 Magnetization transfer was positively correlated with CAG repeat length in segment 1 ($r =$
413 0.641, $p = 0.002$), segment 2 ($r = 0.717$, $p = 0.001$), segment 3 ($r = 0.549$, $p = 0.012$),
414 segment 4 ($r = 0.549$, $p = 0.012$), segment 5 ($r = 0.525$, $p = 0.018$), and segment 6 ($r = 0.513$,
415 $p = 0.021$). After Bonferroni correction the relationship remained significant in segments 1 (p
416 $= 0.014$), 2 ($p = 0.007$) and 4 ($p = 0.007$) (Fig. 6). Partial correlations were carried out to
417 explore the relationships between magnetization transfer and CAG repeat length
418 independently of ICV and disease burden. Even stronger positive associations were now
419 detected; interestingly, the association was now significant also in segment 7, before
420 correction (segment 1: $r = 0.763$, $p = 0.001$, corrected $p = 0.007$; segment 2: $r = 0.879$, $p <$
421 0.001, corrected $p < 0.001$; segment 3: $r = 0.841$, $p < 0.001$, corrected $p < 0.001$; segment 4: r
422 $= 0.83$, $p < 0.001$, corrected $p < 0.001$; segment 5: $r = 0.745$, $p = 0.001$, corrected $p = 0.007$;
423 segment 6: $r = 0.864$, $p < 0.001$, corrected $p < 0.001$; segment 7: $r = 0.5$, $p = 0.048$, corrected
424 $p = 0.336$) (Fig. 5). No significant associations were detected between magnetization transfer
425 scores in each of the 7 callosal segments and DBS.
426
427
428 **Whole-brain analysis with TBCA reveals WM microstructure**
429 **alterations in the posterior CC, the left CST and the right fronto-**
430 **striatal projections**
431
432 Fig. 7A shows the TBCA results. Consistent with the PCA results, a significant reduction in
433 MTR in the patient group was detected, compared to controls, in the posterior portion of the
434 CC [cluster mass ($\sum$ t-score) = 1530, $p < 0.001$ (uncorrected), $p = 0.030$ (FWE-corrected)].
435 Furthermore, a significant increase in FR along most of the left CST was found in patients

[cluster mass (∑ t-score) = 1004, $p < 0.001$ (uncorrected), $p = 0.030$ (FWE-corrected)]. Finally, right-lateralized clusters of significantly higher FA in the patient group were identified in the fronto-striatal projections [cluster mass (∑ t-score) = 956, $p < 0.001$ (uncorrected), $p = 0.03$ (FWE-corrected)].

Fig. 7B plots the relationship between significant microstructure clusters as detected with TBCA for patients. FR in the CST was significantly associated with MTR in the posterior CC ($r = 0.498$, $p = 0.011$, corrected $p = 0.033$) (a scatterplot of the relationship is shown in Fig. 7C), but not with FA in the right fronto-striatal projections ($r = 0.328$, $p = 0.110$, corrected $p = 0.327$). Additionally, MTR was not associated with FA ($r = -0.218$, $p = 0.294$, corrected $p = 0.882$).

Discussion

We carried out a comprehensive tractometry analysis [16–18] of regional differences across the CC in premanifest HD compared to age- and sex-matched healthy controls. By exploiting the ultra-strong magnetic field gradients of the Connectom scanner [8,9], it was possible to better tease apart alterations in myelin/iron content from alterations in axon microstructure [10]. Specifically, although measurements of this *style* could be carried out on any scanner, the Connectom allows the realisation of high b-values (e.g. b= 6000 s/mm2 as used here) with echo times, gradient duration and gradient separation that cannot be achieved with conventional gradients. Such timing parameters allow diffusion-weighted data to be acquired with an SNR per unit time that cannot be attained on other MR scanners at present.

We detected lower MTR, but not axon density, in the callosal isthmus of patients compared to controls. These results are consistent with previous DTI studies reporting microstructural changes in this callosal region in premanifest HD [86,94]. Interestingly, patients presented significantly higher MTR than controls in the callosal rostrum and, overall, MTR was higher in patients than controls in the anterior portions of the CC. Additionally, a positive association was detected between MTR and CAG size, but not DBS, in patients, suggesting a direct link between microstructural alterations and the disease mutation. Finally, a significant interaction effect was detected between group and age on MTR, suggesting that while MTR in this tract is higher in younger patients, the opposite is true for older patients, which likely present increased disease burden.

468 Our findings may be due to a number of different mechanisms. Based on the high
469 correlations reported between magnetization transfer-based measures and histological myelin
470 content [95], our results may suggest that, at least early on in disease progression, the HD
471 mutation is associated with excessive, rather than reduced, myelin production. This might be
472 caused by a pathological increase in myelin-producing oligodendrocytes. In accord with this
473 proposal, previous evidence has suggested that HD gene expression may influence brain cell
474 densities early in the life of gene carriers [31], and that increased CAG repeats are associated
475 with more complex neuronal development, including myelination, across species and
476 ontologically [96]. Additionally, this explanation agrees with findings from neuropathology
477 showing increased density of myelin-producing oligodendrocytes in the brain of premanifest
478 patients [30]. Furthermore *mHTT* directly alters the proliferation property of cultured
479 oligodendrocyte precursor cells (OPCs), with the degree of cell proliferation of OPCs
480 increasing with pathological severity and increasing CAG repeat length [22].
481 As oligodendrocytes are the major iron-containing cells in the adult central nervous system
482 [97], the above studies also support the notion that changes in MTR observed in this study may
483 be driven by iron alterations, and such a proposition is consistent with evidence that changes
484 in iron affect magnetization transfer parameters [98]. Crucially, however, as iron and myelin
485 levels in the brain are tightly related, these two explanations are not mutually exclusive, and
486 further work is needed to uncover the generative mechanism underpinning the present
487 findings. Importantly, in accord with these results, recent evidence from the cross-sectional
488 HD Young Adult Study demonstrated increased R_1 and R_2* values, again suggestive of either
489 increased iron or increased myelin, in the putamen, globus pallidum and external capsule of
490 HD patients more than 20 years away from clinical onset [99].
491 Mutation-related excessive levels of myelin and/or iron early in the disease may come at the
492 cost of detrimental effects later in the disease due to oxidative stress [21,100,101]. Critically, lower
493 MTR in the most posterior callosal areas, through which fibres from the visual system
494 transverse, suggests that these regions are the first to be affected, in agreement with previous
495 evidence [21,37,102]. The visual system is functionally critical early in life, with myelination
496 occurring early and progressing rapidly [103]. Additionally, this system is highly dynamic and is
497 associated with big energetic demands. As metabolic dysfunction and alterations in
498 energetics play important mechanistic roles in HD [104,105], these changes may contribute to
499 early microstructural impairment in this callosal portion. The suggestion for myelin
500 impairment in this callosal segment is consistent with a previous study carried out by our
501 group at 7 Tesla [7], which demonstrated significantly lower myelin water signal fraction in the

posterior callosum of premanifest HD patients. Moreover, this suggestion is in accord with the Demyelination Hypothesis, which argues that early myelinated fibres are more susceptible to myelin disorder in the disease [21].

Overall, we demonstrate measurable and significant differences in callosal magnetization transfer before changes in proxy metrics of axon density can be detected. These changes may reflect early neuronal dysfunction [106] or a CAG-driven neurodevelopmental component to the pathogenesis of HD, as a precursor to the more global neurodegeneration process [22,107–109]. Accordingly, there is increasing evidence that neurodevelopment is affected in HD [96,107] and that such developmental elements of HD are independent of ongoing neurodegeneration [99]. While the present study was not designed to detect HD-associated developmental changes, future studies following young premanifest subjects longitudinally should address the possibility of toxic myelin levels due to pathological CAG repeats size.

The lack of a significant association between MTR changes and DBS in our study contrasts with previous HD research reporting significant relationships between MRI-derived measures and cumulative probability to onset (CPO) [110], a measure similar to DBS. Zhang and colleagues [111], for example, demonstrated that CPO correlated with the neurite density index (NDI) in the callosal body and splenium of HD patients. While MTR and NDI are known to be sensitive to different sub-compartments of tissue (i.e., MTR being more sensitive to myelin and NDI being more sensitive to axon density), it is nevertheless useful to speculate as to why one study found a disease burden *vs* imaging correlation and one did not. First, and foremost, the difference in results may simply reflect heterogeneity of the disease, and the cohorts in the two studies may genuinely have had different underlying microstructural signatures. Second, it may reflect differences in the approaches used to model both microstructure and disease progression in each study. Third, differences in sample sizes across studies (e.g. n = 25 in our study compared to, for example, n = 38 in Zhang et al.[111]) might have an effect on the observed results. Therefore, it is challenging to assert whether any of the above factors, or indeed their combination, underpinned the difference in findings. Importantly, it has to be noted that a study recently published by Johnson et al. [99] also reported the lack of significant associations between DBS and any imaging measures assessed, which included, amongst others, diffusion metrics and proxy measures of myelin and iron content. In their study, Johnson and colleagues highlight that CSF neurofilament light might be a more sensitive and dynamic marker of the disease course, particularly in premanifest HD [99,112].

535 With TBCA, clusters of significantly higher FA were detected in the patient group in the
536 right fronto-striatal projections. Though neurodegenerative disorders have normally been
537 associated with lower FA in major WM pathways, attributed to WM degeneration,
538 demyelination, reduced gliosis or axonal damage as a result of GM loss [113,114], it is possible
539 that selective degeneration of specific WM tracts resulted here in higher anisotropy values
540 and a paradoxical increase in microstructural organization[115]. This suggests that WM
541 degeneration in this area is already present at the premanifest stage of the disease.
542 Importantly, significantly higher FR along most of the left CST was also detected with
543 TBCA. This tract is composed of descending WM fibres, with half of them arising from the
544 primary motor cortex, and is anatomically linked to the basal ganglia [116,117]. From a
545 functional point of view, the CST conducts motor impulses from the brain to the spinal cord,
546 and plays an essential role in voluntary movement [116,117]. Though the hallmark symptom of
547 HD concerns involuntary choreic movements [118], alterations in voluntary movement are also
548 present in premanifest patients [119], thus suggesting that alterations in this tract may play an
549 important role in the disease. Crucially, this is the first time that alterations in this measure
550 have been detected in premanifest patients, pointing to the potential of FR as *in-vivo* MRI
551 marker of premanifest neural changes.
552 Previous studies have demonstrated lower WM volume in the internal capsule of manifest
553 patients [120,121]. Accordingly, the elevated FR detected in this study might reflect the loss of
554 non-neuronal cells, in turn leading to axons being pushed together [122]. Alternatively, such a
555 result might reflect axonal swelling [123]. Consistent with this suggestion, previous evidence
556 demonstrated higher iron levels in the left CST of premanifest patients [99,124], interpreted as
557 indicating an homeostatic increase in oligodendrocytes to repair myelin damage. In turn,
558 myelin damage leads to axon swelling [125]. It might also be that fibre bundles develop
559 differently because of the genetic mutation, and this is consistent with evidence of
560 morphological alterations in the neurons of HD mice, which present smaller diameter
561 dendritic shafts, smaller somatic cross-sectional areas, and decreased diameter of the
562 dendritic fields [126]. Finally, higher FR might reflect the presence of a process of
563 reorganization and compensatory pruning of axons in WM, such as pathologically-driven
564 reduced collateral branching or morphological alterations of individual axons. Consistent
565 with this suggestion, evidence has shown increased coherence of axonal organization in
566 premanifest patients, as suggested by a smaller orientation dispersion index (OD), in tracts
567 surrounding the basal ganglia and in the internal and external capsule [111]. Additionally, the

568 significant association between FR in the CST and MTR in the posterior callosum, further
569 suggests the presence of compensatory mechanisms involving the WM of patients.
570 Finally, the finding of higher FR in the left CST is consistent with the leftward-biased GM
571 loss demonstrated in the striatum of patients [127] and with the leftward asymmetry of brain
572 iron in aging and motor disorders [128,129]. Nevertheless, future studies are needed to determine
573 whether this is an important finding to understand disease pathology. For example, future
574 studies could investigate the longitudinal evolution of changes in FR in patients.
575

576 # Study Limitations and Future Directions

577 To date, only one other study has used extensive microstructural measures in premanifest HD
578 [99]. Moving beyond commonly-available diffusion tensor imaging measures, and using such
579 advanced measurements is essential for understanding the trajectory of WM microstructure
580 alterations across the disease course, which is expected to vary as disease processes change
581 [99,130]. Notably, though much of our understanding of HD pathology will increasingly rely on
582 advanced neuroimaging techniques, it is important to remember and address the
583 shortcomings of these approaches. Accordingly, while it is tempting to assign, unequivocally,
584 a one-to-one correlation between changes in the MRI signal and biological properties, the
585 present findings need to be interpreted with caution.
586 For example, it is important to note that the MTR is influenced by a complex combination of
587 biological factors (including T_1), making it difficult to pinpoint with certainty which
588 pathological processes are responsible for the altered MTR observed in patients in this study.
589 While a change in myelination will result in a change in MTR, a change in MTR may result
590 from other physiological /biophysical changes in the WM (including changes in T_1), making it
591 difficult to separate the effects of reduced macromolecular density because of demyelination
592 and/or axonal loss, iron alterations or increased water because of oedema and/or inflammation
593 [131–134]. Therefore, though an attempt was made to control for confounding elements by, for
594 example, including FWF as a factor in the analyses, and complementing MTR with other
595 microstructure-sensitive metrics, these results require replication in future studies. More
596 specifically, future investigations may benefit from utilising quantitative magnetization
597 transfer[135], myelin water imaging[136] or inhomogeneous magnetization transfer[137] to assess
598 myelin alterations in the premanifest disease stage.
599 A similar methodological consideration needs to be made with regards to the interpretation of
600 FR changes. Specifically, because of the way FR is computed (i.e., the CHARMED model

601 recovers a T2-weighted restricted and hindered diffusion-weighted signal), variation in T_2
602 relaxation (for example because of altered tissue water or myelin content) may be
603 erroneously interpreted as a difference in FR.
604 Additionally, it is challenging to estimate the contribution of smaller axons to the diffusion
605 signal [138]. Though this work utilised ultra-strong gradients (300 mT/m), therefore allowing
606 the contribution of axons with a diameter as small as 3 μm to be assessed [139–141], the majority
607 of axons in the brain have a diameter smaller than 1μm [20,141–143]. Because of this, changes in
608 later myelinating WM areas (such as the anterior portions of the CC), which are characterized
609 by small and thinly myelinated axons, may have not been appropriately reflected by variation
610 in FR. Hence, there is a possibility that increases in MTR observed in the anterior portions of
611 the CC may have reflected decreased axonal density in this area, rather than compensatory
612 remyelination. However, the lack of significant changes in other measures, such as AD or
613 RD, suggests the absence of significant axon changes in the HD sample.
614 To gain increased understanding of the neurobiological underpinnings of FR differences,
615 future studies could investigate disease-associated changes in volume and axon diameter
616 distribution in the CST. Additionally, they might assess apparent fiber density changes at
617 high diffusion-weightings, to increase suppression of the extra-axonal signal. This approach
618 was recently shown to enable a better characterization of microstructural changes, because of
619 the improved correspondence with intra-axonal properties [10,11,144].
620 Finally, our findings were based on a relatively small sample size and warrant replication in
621 larger samples, which could additionally benefit from being assessed longitudinally rather
622 than cross-sectionally, to enable a better understanding of how imaging changes relate to
623 clinical symptoms over time, and evaluate the utility of these metrics as markers of early
624 disease development and progression.
625 Notwithstanding the above limitations, findings from this work highlight the fundamental
626 importance of gaining an enhanced understanding of the mechanisms underlying WM
627 abnormalities in HD. Crucially, our results suggest that microstructure alterations in the
628 disease may reflect CAG-driven neurodevelopmental, rather than neurodegenerative, changes
629 and that expanding intervention strategies to include oligodendroglial targets [25] directly
630 targeting WM pathology may be beneficial for HD.
631
632
633
634

Availability of data and materials

The data analysed during the current study and the respective analysis scripts are available from the corresponding author on reasonable request.

References

1. Scahill RI, Zeun P, Osborne-Crowley K, et al. Biological and clinical characteristics of gene carriers far from predicted onset in the Huntington's disease young adult study (HD-YAS): a cross-sectional analysis. *The Lancet Neurology*. 2020;19(6):502-512.

2. Paulsen JS, Langbehn DR, Stout JC, et al. Detection of Huntington's disease decades before diagnosis: the Predict-HD study. *J Neurol Neurosurg Psychiatry*. 2008;79(8):874-880. doi:10.1136/jnnp.2007.128728

3. Gregory S, Johnson E, Byrne LM, et al. Characterizing White Matter in Huntington's Disease. *Mov Disord Clin Pract*. 2019;7(1):52-60. doi:10.1002/mdc3.12866

4. McColgan P, Seunarine KK, Razi A, et al. Selective vulnerability of Rich Club brain regions is an organizational principle of structural connectivity loss in Huntington's disease. *Brain*. 2015;138(11):3327-3344.

5. McColgan P, Gregory S, Razi A, et al. White matter predicts functional connectivity in premanifest Huntington's disease. *Annals of clinical and translational neurology*. 2017;4(2):106-118.

6. McColgan P, Gregory S, Seunarine KK, et al. Brain Regions Showing White Matter Loss in Huntington's Disease Are Enriched for Synaptic and Metabolic Genes. *Biol Psychiatry*. 2018;83(5):456-465. doi:10.1016/j.biopsych.2017.10.019

7. Casella C, Kleban E, Rosser AE, et al. Multi-compartment analysis of the complex gradient-echo signal quantifies myelin breakdown in premanifest Huntington's disease. *NeuroImage: Clinical*. 2021;30:102658.

8. Jones DK, Alexander DC, Bowtell R, et al. Microstructural imaging of the human brain with a 'super-scanner': 10 key advantages of ultra-strong gradients for diffusion MRI. *NeuroImage*. 2018;182:8-38. doi:10.1016/j.neuroimage.2018.05.047

9. Setsompop K, Kimmlingen R, Eberlein E, et al. Pushing the limits of in vivo diffusion MRI for the Human Connectome Project. *NeuroImage*. 2013;80:220-233. doi:10.1016/j.neuroimage.2013.05.078

10. Kleban E, Tax CMW, Rudrapatna US, Jones DK, Bowtell R. Strong diffusion gradients allow the separation of intra- and extra-axonal gradient-echo signals in the human brain. *NeuroImage*. 2020;217:116793. doi:10.1016/j.neuroimage.2020.116793

11. Genc S, Tax CMW, Raven EP, Chamberland M, Parker GD, Jones DK. Impact of b-value on estimates of apparent fibre density. *Human Brain Mapping*. 2020;41(10):2583-2595. doi:https://doi.org/10.1002/hbm.24964

672 12. Raffelt D, Tournier JD, Rose S, et al. Apparent fibre density: a novel measure for the
673 analysis of diffusion-weighted magnetic resonance images. *Neuroimage*.
674 2012;59(4):3976-3994.

675 13. Pierpaoli C, Basser PJ. Toward a quantitative assessment of diffusion anisotropy. *Magn*
676 *Reson Med*. 1996;36(6):893-906.

677 14. Assaf Y, Basser PJ. Composite hindered and restricted model of diffusion (CHARMED)
678 MR imaging of the human brain. *Neuroimage*. 2005;27(1):48-58.
679 doi:10.1016/j.neuroimage.2005.03.042

680 15. De Santis S, Drakesmith M, Bells S, Assaf Y, Jones DK. Why diffusion tensor MRI does
681 well only some of the time: Variance and covariance of white matter tissue
682 microstructure attributes in the living human brain. *Neuroimage*. 2014;89(100):35-44.
683 doi:10.1016/j.neuroimage.2013.12.003

684 16. Bells S, Cercignani M, Deoni S, et al. Tractometry–comprehensive multi-modal
685 quantitative assessment of white matter along specific tracts. In: Vol 678. ; 2011:1.

686 17. Jones DK, Travis AR, Eden G, Pierpaoli C, Basser PJ. PASTA: pointwise assessment
687 of streamline tractography attributes. *Magnetic Resonance in Medicine: An Official*
688 *Journal of the International Society for Magnetic Resonance in Medicine*.
689 2005;53(6):1462-1467.

690 18. Jones DK, Catani M, Pierpaoli C, et al. Age effects on diffusion tensor magnetic
691 resonance imaging tractography measures of frontal cortex connections in
692 schizophrenia. *Human brain mapping*. 2006;27(3):230-238.

693 19. Luque Laguna PA. Neuroanatomy-based strategies for the statistical analysis of brain
694 imaging and tractography data. Published online 2019.

695 20. Aboitiz F, Scheibel AB, Fisher RS, Zaidel E. Fiber composition of the human corpus
696 callosum. *Brain Res*. 1992;598(1-2):143-153.

697 21. Bartzokis G, Lu PH, Tishler TA, et al. Myelin breakdown and iron changes in
698 Huntington's disease: pathogenesis and treatment implications. *Neurochem Res*.
699 2007;32(10):1655-1664. doi:10.1007/s11064-007-9352-7

700 22. Jin J, Peng Q, Hou Z, et al. Early white matter abnormalities, progressive brain pathology
701 and motor deficits in a novel knock-in mouse model of Huntington's disease. *Hum Mol*
702 *Genet*. 2015;24(9):2508-2527. doi:10.1093/hmg/ddv016

703 23. Simmons DA, Casale M, Alcon B, Pham N, Narayan N, Lynch G. Ferritin accumulation
704 in dystrophic microglia is an early event in the development of Huntington's disease.
705 *Glia*. 2007;55(10):1074-1084.

706 24. Teo RTY, Hong X, Yu-Taeger L, et al. Structural and molecular myelination deficits
707 occur prior to neuronal loss in the YAC128 and BACHD models of Huntington disease.
708 *Hum Mol Genet*. 2016;25(13):2621-2632. doi:10.1093/hmg/ddw122

709 25. Bardile CF, Garcia-Miralles M, Caron NS, et al. Intrinsic mutant HTT-mediated defects
710 in oligodendroglia cause myelination deficits and behavioral abnormalities in

711 Huntington disease. *Proceedings of the National Academy of Sciences*.
712 2019;116(19):9622-9627.

713 26. Xiang Z, Valenza M, Cui L, et al. Peroxisome-proliferator-activated receptor gamma
714 coactivator 1 α contributes to dysmyelination in experimental models of Huntington's
715 disease. *J Neurosci*. 2011;31(26):9544-9553. doi:10.1523/JNEUROSCI.1291-11.2011

716 27. Huang B, Wei W, Wang G, et al. Mutant huntingtin downregulates myelin regulatory
717 factor-mediated myelin gene expression and affects mature oligodendrocytes. *Neuron*.
718 2015;85(6):1212-1226. doi:10.1016/j.neuron.2015.02.026

719 28. Radulescu CI, Garcia-Miralles M, Sidik H, et al. Manipulation of microbiota reveals
720 altered myelination and white matter plasticity in a model of Huntington disease.
721 *bioRxiv*. Published online September 10, 2018. doi:10.1101/413112

722 29. Blockx I, Verhoye M, Van Audekerke J, et al. Identification and characterization of
723 Huntington related pathology: an in vivo DKI imaging study. *Neuroimage*.
724 2012;63(2):653-662. doi:10.1016/j.neuroimage.2012.06.032

725 30. Gómez-Tortosa E, MacDonald ME, Friend JC, et al. Quantitative neuropathological
726 changes in presymptomatic Huntington's disease. *Ann Neurol*. 2001;49(1):29-34.

727 31. Myers RH, Vonsattel JP, Paskevich PA, et al. Decreased Neuronal and Increased
728 Oligodendroglial Densities in Huntington's Disease Caudate Nucleus. *J Neuropathol*
729 *Exp Neurol*. 1991;50(6):729-742. doi:10.1097/00005072-199111000-00005

730 32. Ernst A, Alkass K, Bernard S, et al. Neurogenesis in the Striatum of the Adult Human
731 Brain. *Cell*. 2014;156(5):1072-1083. doi:10.1016/j.cell.2014.01.044

732 33. Aylward EH, Nopoulos PC, Ross CA, et al. Longitudinal change in regional brain
733 volumes in prodromal Huntington disease. *J Neurol Neurosurg Psychiatry*.
734 2011;82(4):405-410. doi:10.1136/jnnp.2010.208264

735 34. Beglinger LJ, Langbehn DR, Duff K, et al. Probability of obsessive and compulsive
736 symptoms in Huntington's disease. *Biol Psychiatry*. 2007;61(3):415-418.
737 doi:10.1016/j.biopsych.2006.04.034

738 35. Ciarmiello A, Cannella M, Lastoria S, et al. Brain white-matter volume loss and glucose
739 hypometabolism precede the clinical symptoms of Huntington's disease. *J Nucl Med*.
740 2006;47(2):215-222.

741 36. Rosas HD, Tuch DS, Hevelone ND, et al. Diffusion tensor imaging in presymptomatic
742 and early Huntington's disease: Selective white matter pathology and its relationship to
743 clinical measures. *Mov Disord*. 2006;21(9):1317-1325. doi:10.1002/mds.20979

744 37. Tabrizi SJ, Langbehn DR, Leavitt BR, et al. Biological and clinical manifestations of
745 Huntington's disease in the longitudinal TRACK-HD study: cross-sectional analysis of
746 baseline data. *Lancet Neurol*. 2009;8(9):791-801. doi:10.1016/S1474-4422(09)70170-X

747 38. Tabrizi SJ, Scahill RI, Durr A, et al. Biological and clinical changes in premanifest and
748 early stage Huntington's disease in the TRACK-HD study: the 12-month longitudinal
749 analysis. *Lancet Neurol*. 2011;10(1):31-42. doi:10.1016/S1474-4422(10)70276-3

750 39. Tabrizi SJ, Reilmann R, Roos RAC, et al. Potential endpoints for clinical trials in
751 premanifest and early Huntington's disease in the TRACK-HD study: analysis of 24
752 month observational data. *Lancet Neurol*. 2012;11(1):42-53. doi:10.1016/S1474-
753 4422(11)70263-0

754 40. Klöppel S, Draganski B, Siebner HR, Tabrizi SJ, Weiller C, Frackowiak RSJ. Functional
755 compensation of motor function in pre-symptomatic Huntington's disease. *Brain*.
756 2009;132(6):1624-1632. doi:10.1093/brain/awp081

757 41. Landwehrmeyer GB, Fitzer-Attas CJ, Giuliano JD, et al. Data analytics from Enroll-HD,
758 a global clinical research platform for Huntington's disease. *Movement disorders*
759 *clinical practice*. 2017;4(2):212-224.

760 42. Paulsen JS, Miller AC, Hayes T, Shaw E. Chapter 6 - Cognitive and behavioral changes
761 in Huntington disease before diagnosis. In: Feigin AS, Anderson KE, eds. *Handbook of*
762 *Clinical Neurology*. Vol 144. Huntington Disease. Elsevier; 2017:69-91.
763 doi:10.1016/B978-0-12-801893-4.00006-7

764 43. Paulsen JS, Long JD, Johnson HJ, et al. Clinical and Biomarker Changes in Premanifest
765 Huntington Disease Show Trial Feasibility: A Decade of the PREDICT-HD Study.
766 *Front Aging Neurosci*. 2014;6:78. doi:10.3389/fnagi.2014.00078

767 44. Paulsen JS, Long JD, Ross CA, et al. Prediction of manifest Huntington's disease with
768 clinical and imaging measures: a prospective observational study. *Lancet Neurol*.
769 2014;13(12):1193-1201. doi:10.1016/S1474-4422(14)70238-8

770 45. Pirogovsky E, Goldstein J, Peavy G, Jacobson MW, Corey-Bloom J, Gilbert PE.
771 Temporal order memory deficits prior to clinical diagnosis in Huntington's disease.
772 *Journal of the International Neuropsychological Society: JINS*. 2009;15(5):662.

773 46. Stout JC, Paulsen JS, Queller S, et al. Neurocognitive signs in prodromal Huntington
774 disease. *Neuropsychology*. 2011;25(1):1-14. doi:10.1037/a0020937

775 47. Stout JC, Jones R, Labuschagne I, et al. Evaluation of longitudinal 12 and 24 month
776 cognitive outcomes in premanifest and early Huntington's disease. *J Neurol Neurosurg*
777 *Psychiatry*. 2012;83(7):687-694. doi:10.1136/jnnp-2011-301940

778 48. Hamilton JM, Salmon DP, Corey-Bloom J, et al. Behavioural abnormalities contribute
779 to functional decline in Huntington's disease. *J Neurol Neurosurg Psychiatry*.
780 2003;74(1):120-122. doi:10.1136/jnnp.74.1.120

781 49. Nehl C, Paulsen JS, Huntington Study Group. Cognitive and psychiatric aspects of
782 Huntington disease contribute to functional capacity. *J Nerv Ment Dis*. 2004;192(1):72-
783 74. doi:10.1097/01.nmd.0000106004.67587.57

784 50. Williams JK, Barnette JJ, Reed D, et al. Development of the Huntington Disease Family
785 Concerns and Strategies Survey From Focus Group Data. *J Nurs Meas*. 2010;18(2):83-
786 99.

787 51. Nasreddine ZS, Phillips NA, Bédirian V, et al. The Montreal Cognitive Assessment,
788 MoCA: A Brief Screening Tool For Mild Cognitive Impairment. *Journal of the*

American Geriatrics Society. 2005;53(4):695-699. doi:10.1111/j.1532-5415.2005.53221.x

52. Wechsler D. Test of premorbid functioning. UK version (TOPF UK). *UK: Pearson Corporation*. Published online 2011.

53. Unified Huntington's disease rating scale: Reliability and consistency. *Movement Disorders*. 1996;11(2):136-142. doi:10.1002/mds.870110204

54. Kieburtz K, Penney JB, Corno P, et al. Unified Huntington's disease rating scale: reliability and consistency. *Neurology*. 2001;11(2):136-142.

55. Siesling S, Van Vugt JP, Zwinderman KA, Kieburtz K, Roos RA. Unified Huntington's disease rating scale: a follow up. *Movement disorders: official journal of the Movement Disorder Society*. 1998;13(6):915-919.

56. Kirchner WK. Age differences in short-term retention of rapidly changing information. *Journal of experimental psychology*. 1958;55(4):352.

57. Wechsler D. Wechsler Adult Intelligence Scale—Revised UK. *New York: Psychological Corporation;*. Published online January 1, 1997.

58. Della Sala S, Gray C, Baddeley A, Wilson L. Visual Patterns Test: A test of short-term visual recall. *Thames Valley Test Company*. 1997;40.

59. Reitan RM, Davison LA. *Clinical Neuropsychology: Current Status and Applications.* VH Winston & Sons; 1974.

60. Mueller ST, Piper BJ. The psychology experiment building language (PEBL) and PEBL test battery. *Journal of neuroscience methods*. 2014;222:250-259.

61. Metzler-Baddeley C, Cantera J, Coulthard E, Rosser A, Jones DK, Baddeley RJ. Improved Executive Function and Callosal White Matter Microstructure after Rhythm Exercise in Huntington's Disease. *J Huntingtons Dis*. 2014;3(3):273-283. doi:10.3233/JHD-140113

62. Freeman GL. The relationship between performance level and bodily activity level. *Journal of Experimental Psychology*. 1940;26(6):602-608. doi:10.1037/h0056767

63. Tournier JD, Calamante F, Connelly A. Determination of the appropriate b value and number of gradient directions for high-angular-resolution diffusion-weighted imaging. *NMR in Biomedicine*. 2013;26(12):1775-1786. doi:10.1002/nbm.3017

64. Smith SM, Jenkinson M, Woolrich MW, et al. Advances in functional and structural MR image analysis and implementation as FSL. *Neuroimage*. 2004;23 Suppl 1:S208-219. doi:10.1016/j.neuroimage.2004.07.051

65. Tournier JD, Smith R, Raffelt D, et al. MRtrix3: A fast, flexible and open software framework for medical image processing and visualisation. *NeuroImage*. 2019;202:116137. doi:10.1016/j.neuroimage.2019.116137

66. Avants BB, Tustison NJ, Song G, Cook PA, Klein A, Gee JC. A reproducible evaluation of ANTs similarity metric performance in brain image registration. *Neuroimage*. 2011;54(3):2033-2044. doi:10.1016/j.neuroimage.2010.09.025

67. Veraart J, Fieremans E, Novikov DS. Diffusion MRI noise mapping using random matrix theory. *Magn Reson Med*. 2016;76(5):1582-1593. doi:10.1002/mrm.26059

68. Sairanen V, Leemans A, Tax CMW. Fast and accurate Slicewise OutLIer Detection (SOLID) with informed model estimation for diffusion MRI data. *Neuroimage*. 2018;181:331-346. doi:10.1016/j.neuroimage.2018.07.003

69. Vos SB, Tax CMW, Luijten PR, Ourselin S, Leemans A, Froeling M. The importance of correcting for signal drift in diffusion MRI. *Magn Reson Med*. 2017;77(1):285-299. doi:10.1002/mrm.26124

70. Andersson JLR, Skare S, Ashburner J. How to correct susceptibility distortions in spin-echo echo-planar images: application to diffusion tensor imaging. *Neuroimage*. 2003;20(2):870-888. doi:10.1016/S1053-8119(03)00336-7

71. Andersson JLR, Sotiropoulos SN. An integrated approach to correction for off-resonance effects and subject movement in diffusion MR imaging. *Neuroimage*. 2016;125:1063-1078. doi:10.1016/j.neuroimage.2015.10.019

72. Kellner E, Dhital B, Kiselev VG, Reisert M. Gibbs-ringing artifact removal based on local subvoxel-shifts. *Magn Reson Med*. 2016;76(5):1574-1581. doi:10.1002/mrm.26054

73. Tustison NJ, Avants BB, Cook PA, et al. N4ITK: improved N3 bias correction. *IEEE Trans Med Imaging*. 2010;29(6):1310-1320. doi:10.1109/TMI.2010.2046908

74. Glasser MF, Sotiropoulos SN, Wilson JA, et al. The minimal preprocessing pipelines for the Human Connectome Project. *Neuroimage*. 2013;80:105-124. doi:10.1016/j.neuroimage.2013.04.127

75. Rudrapatna U, Parker GD, Roberts J, Jones DK. A comparative study of gradient nonlinearity correction strategies for processing diffusion data obtained with ultra-strong gradient MRI scanners. *Magnetic Resonance in Medicine*. 2021;85(2):1104-1113. doi:https://doi.org/10.1002/mrm.28464

76. Ben-Amitay S, Jones DK, Assaf Y. Motion correction and registration of high b-value diffusion weighted images. *Magn Reson Med*. 2012;67(6):1694-1702. doi:10.1002/mrm.23186

77. Jenkinson M, Smith S. A global optimisation method for robust affine registration of brain images. *Medical image analysis*. 2001;5(2):143-156.

78. Wasserthal J, Neher P, Maier-Hein KH. TractSeg - Fast and accurate white matter tract segmentation. *NeuroImage*. 2018;183:239-253. doi:10.1016/j.neuroimage.2018.07.070

79. Jeurissen B, Tournier JD, Dhollander T, Connelly A, Sijbers J. Multi-tissue constrained spherical deconvolution for improved analysis of multi-shell diffusion MRI data. *NeuroImage*. 2014;103:411-426.

80. Team Rs. RStudio: integrated development for R. *RStudio, Inc, Boston, MA URL http://www rstudio com*. 2015;42:14.

81. Armonk N. IBM Corp. SPSS Statistics for windows, Version 20.0. Published online 2011.

82. Hayes AF. *Introduction to Mediation, Moderation, and Conditional Process Analysis: A Regression-Based Approach*. Guilford publications; 2017.

83. Nichols T, Holmes A. SnPM-Statistical NonParametric Mapping: A Toolbox for SPM. Published online 2014.

84. Steventon J. Characterising the structural brain changes in Huntington's disease using translational neuroimaging. Published online November 2014. Accessed June 4, 2020. http://orca.cf.ac.uk/71204/

85. Geeraert BL, Chamberland M, Lebel RM, Lebel C. Multimodal principal component analysis to identify major features of white matter structure and links to reading. *PLOS ONE*. 2020;15(8):e0233244. doi:10.1371/journal.pone.0233244

86. Phillips O, Sanchez-Castaneda C, Elifani F, et al. Tractography of the Corpus Callosum in Huntington's Disease. *PLOS ONE*. 2013;8(9):e73280. doi:10.1371/journal.pone.0073280

87. Chamberland M, Raven EP, Genc S, et al. Dimensionality reduction of diffusion MRI measures for improved tractometry of the human brain. *NeuroImage*. 2019;200:89-100. doi:10.1016/j.neuroimage.2019.06.020

88. Wickham H. Tidy data. *Journal of Statistical Software*. 2014;59(10):1-23.

89. Metzler-Baddeley C, Foley S, de Santis S, et al. Dynamics of White Matter Plasticity Underlying Working Memory Training: Multimodal Evidence from Diffusion MRI and Relaxometry. *J Cogn Neurosci*. 2017;29(9):1509-1520. doi:10.1162/jocn_a_01127

90. Smith SM, Jenkinson M, Johansen-Berg H, et al. Tract-based spatial statistics: Voxelwise analysis of multi-subject diffusion data. *NeuroImage*. 2006;31(4):1487-1505. doi:10.1016/j.neuroimage.2006.02.024

91. Winkler AM, Ridgway GR, Webster MA, Smith SM, Nichols TE. Permutation inference for the general linear model. *Neuroimage*. 2014;92:381-397. doi:10.1016/j.neuroimage.2014.01.060

92. Bullmore ET, Suckling J, Overmeyer S, Rabe-Hesketh S, Taylor E, Brammer MJ. Global, voxel, and cluster tests, by theory and permutation, for a difference between two groups of structural MR images of the brain. *IEEE Trans Med Imaging*. 1999;18(1):32-42. doi:10.1109/42.750253

93. Bourbon-Teles J, Bells S, Jones DK, Coulthard E, Rosser A, Metzler-Baddeley C. Myelin Breakdown in Human Huntington's Disease: Multi-Modal Evidence from Diffusion MRI and Quantitative Magnetization Transfer. *Neuroscience*. 2019;403:79-92. doi:10.1016/j.neuroscience.2017.05.042

94. Di Paola M, Phillips OR, Sanchez-Castaneda C, et al. MRI measures of corpus callosum iron and myelin in early Huntington's disease. *Hum Brain Mapp*. 2014;35(7):3143-3151. doi:10.1002/hbm.22391

95. Mancini M, Karakuzu A, Cohen-Adad J, Cercignani M, Nichols TE, Stikov N. An interactive meta-analysis of MRI biomarkers of myelin. Jbabdi S, Baker CI, Jbabdi S, Does M, eds. *eLife*. 2020;9:e61523. doi:10.7554/eLife.61523

96. van der Plas E, Langbehn DR, Conrad AL, et al. Abnormal brain development in child and adolescent carriers of mutant huntingtin. *Neurology*. 2019;93(10):e1021-e1030.

97. Connor JR, Menzies SL. Cellular management of iron in the brain. *Journal of the Neurological Sciences*. 1995;134:33-44. doi:10.1016/0022-510X(95)00206-H

98. Birkl C, Birkl-Toeglhofer AM, Kames C, et al. The influence of iron oxidation state on quantitative MRI parameters in post mortem human brain. *NeuroImage*. 2020;220:117080. doi:10.1016/j.neuroimage.2020.117080

99. Johnson EB, Parker CS, Scahill RI, et al. Altered iron and myelin in premanifest Huntington's Disease more than 20 years before clinical onset: Evidence from the cross-sectional HD Young Adult Study. *EBioMedicine*. 2021;65:103266.

100. Bartzokis G, Cummings J, Perlman S, Hance DB, Mintz J. Increased basal ganglia iron levels in Huntington disease. *Arch Neurol*. 1999;56(5):569-574.

101. Bartzokis G, Tishler TA. MRI evaluation of basal ganglia ferritin iron and neurotoxicity in Alzheimer's and Huntingon's disease. *Cell Mol Biol (Noisy-le-grand)*. 2000;46(4):821-833.

102. Coppen EM, van der Grond J, Hafkemeijer A, Rombouts SARB, Roos RAC. Early grey matter changes in structural covariance networks in Huntington's disease. *NeuroImage: Clinical*. 2016;12:806-814. doi:10.1016/j.nicl.2016.10.009

103. Yakovlev P. The myelogenetic cycles of regional maturation of the brain. *Regional development of the brain in early life*. Published online 1967:3-70.

104. Beal MF. Mitochondria take center stage in aging and neurodegeneration. *Annals of Neurology: Official Journal of the American Neurological Association and the Child Neurology Society*. 2005;58(4):495-505.

105. Browne SE. Mitochondria and Huntington's disease pathogenesis: insight from genetic and chemical models. *Annals of the New York Academy of Sciences*. 2008;1147(1):358-382.

106. Rosas HD, Lee SY, Bender AC, et al. Altered white matter microstructure in the corpus callosum in Huntington's disease: implications for cortical "disconnection." *Neuroimage*. 2010;49(4):2995-3004.

107. Barnat M, Capizzi M, Aparicio E, et al. Huntington's disease alters human neurodevelopment. *Science*. 2020;369(6505):787-793. doi:10.1126/science.aax3338

108. Nopoulos PC, Aylward EH, Ross CA, et al. Cerebral cortex structure in prodromal Huntington disease. *Neurobiology of disease*. 2010;40(3):544-554.

109. Phillips O, Squitieri F, Sanchez-Castaneda C, et al. Deep White Matter in Huntington's Disease. *PLOS ONE*. 2014;9(10):e109676. doi:10.1371/journal.pone.0109676

110. Langbehn DR, Brinkman RR, Falush D, Paulsen JS, Hayden MR, International Huntington's Disease Collaborative Group. A new model for prediction of the age of onset and penetrance for Huntington's disease based on CAG length. *Clin Genet*. 2004;65(4):267-277. doi:10.1111/j.1399-0004.2004.00241.x

111. Zhang J, Gregory S, Scahill RI, et al. In vivo characterization of white matter pathology in premanifest huntington's disease. *Annals of Neurology*. 2018;84(4):497-504. doi:10.1002/ana.25309

112. Byrne LM, Rodrigues FB, Johnson EB, et al. Evaluation of mutant huntingtin and neurofilament proteins as potential markers in Huntington's disease. *Science Translational Medicine*. 2018;10(458):eaat7108.

113. Assaf Y. Can we use diffusion MRI as a bio-marker of neurodegenerative processes? *Bioessays*. 2008;30(11-12):1235-1245.

114. Concha L, Gross DW, Wheatley BM, Beaulieu C. Diffusion tensor imaging of time-dependent axonal and myelin degradation after corpus callosotomy in epilepsy patients. *Neuroimage*. 2006;32(3):1090-1099.

115. Douaud G, Behrens TE, Poupon C, et al. In vivo evidence for the selective subcortical degeneration in Huntington's disease. *NeuroImage*. 2009;46(4):958-966. doi:10.1016/j.neuroimage.2009.03.044

116. Kandel ER, Schwartz JH, Jessell TM, Department of Biochemistry and Molecular Biophysics Thomas Jessell, Siegelbaum S, Hudspeth A. *Principles of Neural Science*. Vol 4. McGraw-hill New York; 2000.

117. Schultz SK. Principles of neural science. *American Journal of Psychiatry*. 2001;158(4):662-662.

118. Folstein SE. *Huntington's Disease: A Disorder of Families.* Johns Hopkins University Press; 1989.

119. Rowe KC, Paulsen JS, Langbehn DR, et al. Self-paced timing detects and tracks change in prodromal Huntington disease. *Neuropsychology*. 2010;24(4):435.

120. Fennema-Notestine C, Archibald S, Jacobson M, et al. In vivo evidence of cerebellar atrophy and cerebral white matter loss in Huntington disease. *Neurology*. 2004;63(6):989-995.

121. Nave RD, Ginestroni A, Tessa C, et al. Regional Distribution and Clinical Correlates of White Matter Structural Damage in Huntington Disease: A Tract-Based Spatial Statistics Study. *American Journal of Neuroradiology*. 2010;31(9):1675-1681. doi:10.3174/ajnr.A2128

122. Rattray I, Smith EJ, Crum WR, et al. Correlations of Behavioral Deficits with Brain Pathology Assessed through Longitudinal MRI and Histopathology in the R6/1 Mouse Model of Huntington's Disease. *PLOS ONE*. 2013;8(12):e84726. doi:10.1371/journal.pone.0084726

123. Marangoni M, Adalbert R, Janeckova L, et al. Age-related axonal swellings precede other neuropathological hallmarks in a knock-in mouse model of Huntington's disease. *Neurobiology of Aging*. 2014;35(10):2382-2393. doi:10.1016/j.neurobiolaging.2014.04.024

124. Phillips O, Squitieri F, Sanchez-Castaneda C, et al. The Corticospinal Tract in Huntington's Disease. *Cerebral Cortex*. 2015;25(9):2670-2682. doi:10.1093/cercor/bhu065

125. Payne SC, Bartlett CA, Harvey AR, Dunlop SA, Fitzgerald M. Myelin Sheath Decompaction, Axon Swelling, and Functional Loss during Chronic Secondary Degeneration in Rat Optic Nerve. *Invest Ophthalmol Vis Sci*. 2012;53(10):6093-6101. doi:10.1167/iovs.12-10080

126. Klapstein GJ, Fisher RS, Zanjani H, et al. Electrophysiological and morphological changes in striatal spiny neurons in R6/2 Huntington's disease transgenic mice. *Journal of neurophysiology*. 2001;86(6):2667-2677.

127. Muhlau M, Gaser C, Wohlschager A. Striatal atrophy in Huntington's disease is leftward biased. In: Vol 120. ; 2007.

128. Langkammer C, Krebs N, Goessler W, et al. Quantitative MR imaging of brain iron: a postmortem validation study. *Radiology*. 2010;257(2):455-462.

129. Xu X, Wang Q, Zhang M. Age, gender, and hemispheric differences in iron deposition in the human brain: an in vivo MRI study. *Neuroimage*. 2008;40(1):35-42.

130. Lommers E, Simon J, Reuter G, et al. Multiparameter MRI quantification of microstructural tissue alterations in multiple sclerosis. *NeuroImage: Clinical*. 2019;23:101879. doi:10.1016/j.nicl.2019.101879

131. Deloire-Grassin M, Brochet B, Quesson B, et al. In vivo evaluation of remyelination in rat brain by magnetization transfer imaging. *Journal of the neurological sciences*. 2000;178(1):10-16.

132. Dousset V, Grossman RI, Ramer KN, et al. Experimental allergic encephalomyelitis and multiple sclerosis: lesion characterization with magnetization transfer imaging. *Radiology*. 1992;182(2):483-491.

133. Dousset V, Brochet B, Vital A, et al. Lysolecithin-induced demyelination in primates: preliminary in vivo study with MR and magnetization transfer. *American journal of neuroradiology*. 1995;16(2):225-231.

134. Gareau PJ, Rutt BK, Karlik SJ, Mitchell JR. Magnetization transfer and multicomponent T2 relaxation measurements with histopathologic correlation in an experimental model of MS. *Journal of Magnetic Resonance Imaging: An Official Journal of the International Society for Magnetic Resonance in Medicine*. 2000;11(6):586-595.

135. Henkelman RM, Huang X, Xiang QS, Stanisz GJ, Swanson SD, Bronskill MJ. Quantitative interpretation of magnetization transfer. *Magn Reson Med*. 1993;29(6):759-766.

136. MacKay AL, Laule C. Magnetic Resonance of Myelin Water: An in vivo Marker for Myelin. *Brain Plast*. 2(1):71-91. doi:10.3233/BPL-160033

137. Ercan E, Varma G, Mädler B, et al. Microstructural correlates of 3D steady-state inhomogeneous magnetization transfer (ihMT) in the human brain white matter assessed by myelin water imaging and diffusion tensor imaging. *Magnetic Resonance in Medicine*. 2018;80(6):2402-2414. doi:10.1002/mrm.27211

138. Drakesmith M, Harms R, Rudrapatna SU, Parker GD, Evans CJ, Jones DK. Estimating axon conduction velocity in vivo from microstructural MRI. *NeuroImage*. 2019;203:116186.

139. Drobnjak I, Zhang H, Ianuş A, Kaden E, Alexander DC. PGSE, OGSE, and sensitivity to axon diameter in diffusion MRI: insight from a simulation study. *Magnetic resonance in medicine*. 2016;75(2):688-700.

140. Nilsson M, Lasič S, Drobnjak I, Topgaard D, Westin C. Resolution limit of cylinder diameter estimation by diffusion MRI: The impact of gradient waveform and orientation dispersion. *NMR in Biomedicine*. 2017;30(7):e3711.

141. Sepehrband F, Alexander DC, Kurniawan ND, Reutens DC, Yang Z. Towards higher sensitivity and stability of axon diameter estimation with diffusion-weighted MRI. *NMR in Biomedicine*. 2016;29(3):293-308.

142. Caminiti R, Carducci F, Piervincenzi C, et al. Diameter, length, speed, and conduction delay of callosal axons in macaque monkeys and humans: comparing data from histology and magnetic resonance imaging diffusion tractography. *Journal of Neuroscience*. 2013;33(36):14501-14511.

143. Liewald D, Miller R, Logothetis N, Wagner HJ, Schüz A. Distribution of axon diameters in cortical white matter: an electron-microscopic study on three human brains and a macaque. *Biological cybernetics*. 2014;108(5):541-557.

144. McKinnon ET, Jensen JH. Measuring intra-axonal T2 in white matter with direction-averaged diffusion MRI. *Magnetic Resonance in Medicine*. 2019;81(5):2985-2994. doi:https://doi.org/10.1002/mrm.27617

Tables and Figures

Table 1. Summary of participants' demographic and clinical background information.

	HD patients	Controls	p-value

Gender male/female (%)	15(60)/ 10(40)	14(56)/ 11(44)	p > 0.05
Mean age (years) (SD, range)	42.04 (12.7, 21-70)	43.19 (12.6, 27-71)	p > 0.05
Mean TOPFUK IQ (SD, range)	116.16 (10.2, 98-137.4)	124.96 (6.9, 109-135.4)	**p = 0.003**
Mean MoCA score (SD, range)	27.92 (2.1, 24-30)	28.2 (1.8, 26-30)	p > 0.05
Mean CAG (SD, range)	41.4 (2.1, 37-45)	-	-
Mean DBS (SD, range)	235.94 (84.5, 61.5-450)	-	-
Mean TFC (SD, range)	12.863 (0.4, 12-13	-	-
Mean TMS (SD, range)	3.3 (4.8, 0-18)	-	-
Mean DCL (SD, range)	0.91 (1.3, 0-3)	-	-

TOPFUK FSIQ = verbal IQ estimate based on the Test of Premorbid Functioning, UK version. There was a significant difference between patients and controls in TOPFUK FSIQ, with patients presenting significantly lower premorbid IQ. MoCA = Montreal Cognitive Assessment out of 30 (the higher the score the better the performance). MoCA scores for patients and controls ranged between 23 and 30. A score of 26 or over is generally considered to be normal, while an average score of 22.1 has been reported in people with mild cognitive impairment [51]*. There was no significant difference in this test between the two groups. Two individuals with CAG repeats of 38 were included in the current study. Although these individuals can be considered "affected", they may have a lower risk of becoming symptomatic within their life span; DBS = Disease Burden Score, calculated as follows: DBS = age × (CAG-35.5); TMS = Total Motor Score out of 124 from "UHDRS Motor Diagnostic Confidence (Motor) – the higher the score, the more impaired the performance. Based on TMS scores, all patients were at the premanifest disease stage. DCL = Diagnostic Confidence Level (normal/no abnormalities = 0, non-specific motor abnormalities = 1, motor abnormalities that may be signs of HD = 2, motor abnormalities that are likely signs of HD = 3, motor abnormalities that are unequivocal signs of HD = 4). Only participants with diagnostic confidence level ratings < 4 were included in the current report. However, based on DCL scores, some of the patients (n = 4) presented with some motor abnormalities.*

Table 2. Cognitive outcome variables employed to create a composite cognitive score to assess disease-related brain-function relationships. *Tasks descriptions are provided, outcome variables and cognitive domains assessed are summarized.*

Task	Computerized/paper & pencil	Description	Outcome variable	Cognitive domain assessed
N-back [56]	Computerized	Participants were presented with a series of letters, three seconds apart, and asked to judge whether the current letter matched the previous letter (1-back condition) or the letter presented 2 letters back (2-back condition). The 1-back and 2-back conditions were presented separately in 20 randomly ordered trials. Participants made responses manually by pressing on the letter "A" on the keyboard. No responses were required for non-targets.	Percentage of correct responses in the 1-back and 2-back condition	Encoding, temporary storage and updating of stored information with new upcoming information, inhibition of irrelevant items
Digit Span Test from the WAIS-R [57]	Computerized	Participants were presented with a series of numbers that appeared on the screen one after another. They were required to recall the sequence of numbers by entering them on the keyboard. If the participant could successfully reproduce the series of numbers, they were then presented with a longer series of numbers. Participants continued to receive longer series of numbers until they could no longer repeat them back correctly. The starting list length was 3, and the longest list length possible was 10. The discontinuation criterion was 2 wrong responses.	Maximum span of digits recalled	Verbal working memory capacity
Visual Patterns Test [58]	Paper and pencil	Participants were shown a checkerboard-like grid, with the squares in the grid each randomly coloured. This pattern was displayed for 3 seconds and is then removed. Subjects were then shown a blank grid and were asked to	Maximum grid size recalled correctly	Spatial working memory capacity

		reproduce each grid. The number of items was sequentially increased. Participants were given unlimited time to reproduce the shapes being viewed.		
Speeded Finger Tapping Task [59]	Computerized	Participants were instructed to form a fist shape with their dominant hand, with their fingernails touching down in front of the keyboard space bar. They were then instructed to extend their index finger in order to contact the "space" bar on the keyboard, and to move only their index finger to tap the space bar as quickly as possible.	Mean number of taps over 3 trials	Motor speed
Stroop Interference, Word Reading and Colour Naming [53–55]	Paper and pencil	For the Stroop Reading and Colour Naming, participants had to name colours (e.g., red, green, blue) and read the words for colours in black ink. For the Stroop Interference, participants had to read words of colours (e.g. red, green blue) where the word colour was written in a different colour ink (Stroop Interference).	Number of correct responses	Ability to inhibit cognitive interference, selective attention capacity and skills, processing speed, motor control
Phonetic and Category Verbal Fluency [53–55]	Paper and pencil	In the Phonetic Verbal Fluency task participants had to spontaneously produce words orally within a fixed time span (60 seconds), beginning with a certain letter. In the Category Verbal Fluency, words had to be produced according to semantic constraints (e.g. animals, fruits, vegetables).	Number of correctly generated words within 60 seconds	Working memory, cognitive inhibition, switching ability and language ability including lexical knowledge and lexical retrieval ability

Trail Making (part A & part B) [53–55]	Paper and pencil	In part A, participants were asked to connect 25 randomly arrayed dots in numerical order, whereas in part B they were asked to connect dots alternating between numbers and letters in alphabetical order.	Time needed to complete the task	Visual attention, task switching, speed of processing, mental flexibility
Symbol Digit Modality [53–55]	Paper and pencil	Using a reference key, participant had 90 seconds to pair specific numbers with given geometric figures.	Number of correct responses achieved in 90 seconds	Attention, perceptual speed, motor speed, and visual scanning

Table 3. Scan parameters.

	T_1-w	**DTI**	**CHARMED**	**MT**
Pulse sequence	MPRAGE	SE\EPI	SE\EPI	Turbo FLASH
Matrix size	256×256	495×495	495×495	128 × 128 ×104
FoV (mm)	256	990	990	220 × 220 × 179
Slice thickness (mm)	1	2	2	1.72
TE,TR (ms)	2, 2300	59, 3000	59, 3000	2.1, 60
Off-resonance pulses (Hz/°)	-	-	-	1200/333
Flip angles (°)	9	90	90	5

All sequences were acquired at 3 Tesla with ultra-strong gradients. For each of the sequences, the main acquisition parameters are provided. T_1-w: T_1-weighted; MT: magnetization transfer; MPRAGE: Magnetization prepared - rapid gradient echo; SE: spin-echo; EPI: echo-planar imaging; FoV: field of view; TE: echo time; TR: repetition time.

1086 *Table 4. Correlations of magnetization transfer scores with cognitive component scores, CAG*
1087 *repeat-length and DBS.*

1088

Magnetization transfer	Composite cognitive scores
Segment 1	r = 0.527 (p = 0.032, corrected p = 0.211)
Segment 2	r = 0.559 (p = 0.023, corrected p = 0.141)
Segment 3	r = 0.491 (p = 0.042, corrected p = 0.282)
Segment 4	r = 0.494 (p = 0.054, corrected p = 0.351)
Segment 5	r = 0.451 (p = 0.073, **corrected p = 0.049**)
Segment 6	r = 0.323 (p = 0.03, corrected p = 0.213)
Segment 7	r = -0.098 (p = 0.71, corrected p = 1)
	CAG repeat length
Segment 1	r = 0.641 (p = 0.002, **corrected p = 0.014**), partial correlation: r = 0.763 (p = 0.001, **corrected p = 0.007**)
Segment 2	r = 0.717 (p = 0.001, **corrected p = 0.007),** partial correlation: r = 0.879 (p < 0.001, **corrected p < 0.001**)
Segment 3	r = 0.549 (p = 0.012, corrected p = 0.084), partial correlation: r = 0.841 (p < 0.001, **corrected p < 0.001**)
Segment 4	r = 0.71 (p = 0.001, **corrected p = 0.007**), partial correlation: r = 0.831 (p < 0.001, **corrected p < 0.001**)
Segment 5	r = 0.525 (p = 0.018, corrected p = 0.126), partial correlation: r = 0.745 (p = 0.001, **corrected p = 0.007**)
Segment 6	r = 0.513 (p = 0.021, corrected p =0.147), partial correlation: r = 0.864 (p < 0.001, **corrected p < 0.001**)
Segment 7	r = 0.107 (p = 0.663, corrected p = 1), partial correlation: r = 0.5 (p = 0.048, corrected p = 0.336)
	DBS
Segment 1	r = -0.04 (p = 0.853, corrected p = 1)
Segment 2	r = 0.08 (p = 0.697, corrected p = 1)
Segment 3	r = 0.003 (p = 0.986, corrected p = 1)
Segment 4	r = 0.071 (p = 0.739, corrected p = 1)

Segment 5	r = 0.048 (p = 0.824, corrected p =1)
Segment 6	r = -0.12 (p = 0.642, corrected p = 1)
Segment 7	r = -0.09 (p = 0.662, corrected p = 1)

Correlation coefficients that were significant after Bonferroni correction are highlighted in bold. Trends, defined as correlations significant at the uncorrected level, are highlighted in italics.

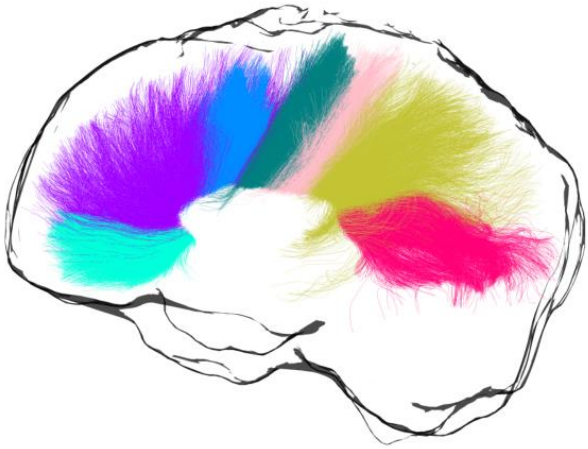

	Segment	Anatomical label	Cortical region
	1	Rostrum	Caudal/orbital prefrontal, inferior premotor
	2	Genu	Prefrontal
	3	Rostral body	Premotor, supplementary motor
	4	Anterior midbody	Motor
	5	Posterior midbody	Somaesthetic, posterior parietal
	6	Isthmus	Superior temporal, posterior parietal
	7	Splenium	Occipital, inferior temporal

Figure 1. Callosal segmentation.

For each segment, the corresponding anatomical label is reported, together with the cortical area it connects to.

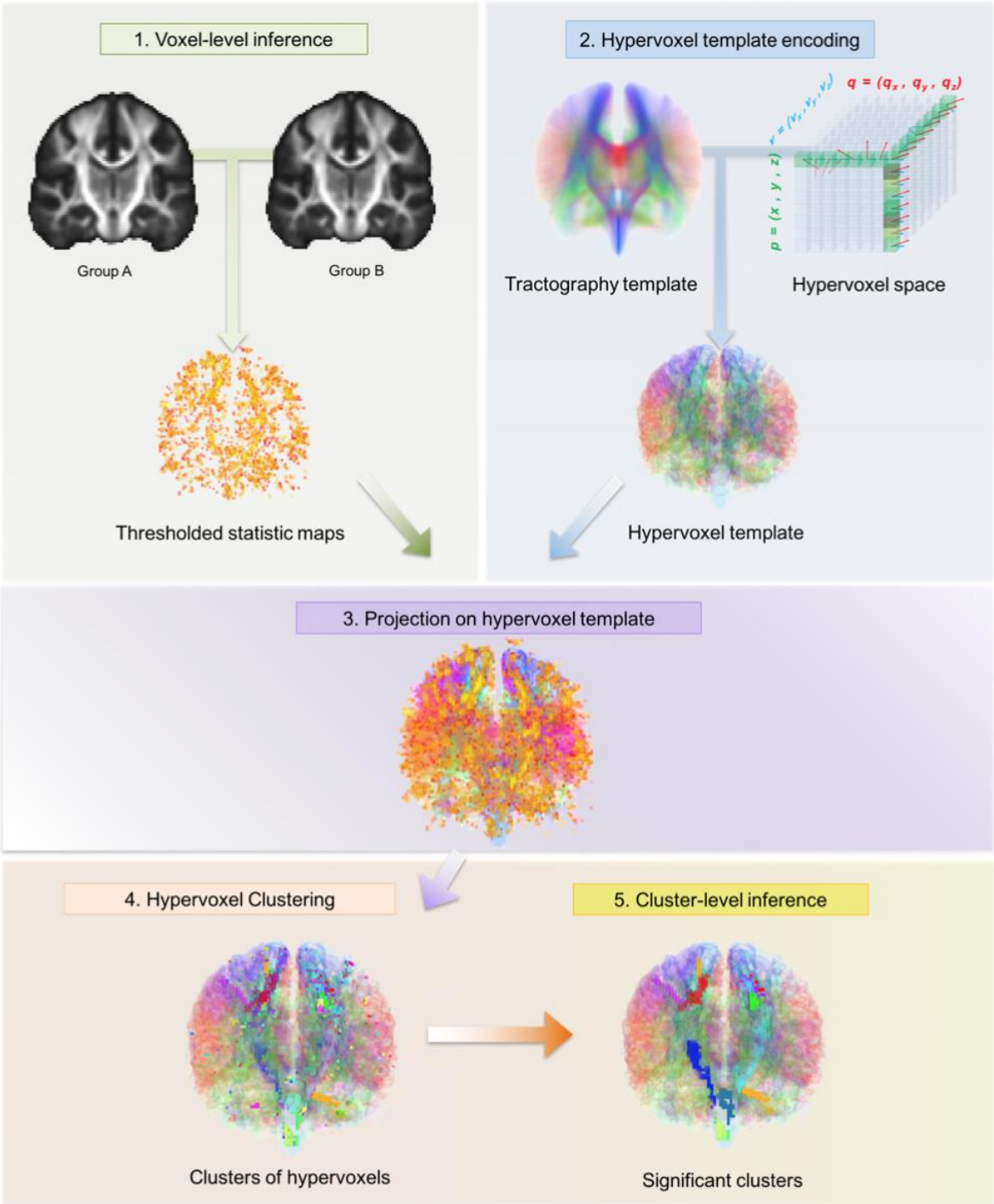

Figure 2. The TBCA analysis pipeline.

After all images have been normalized to a common anatomical space, statistics maps are produced based on the voxel-level analysis of the data; this is done by using a non-parametric approach based on a permutation test strategy [91]. The statistic maps are thresholded by a value of p = 0.01. Next, the significant voxel level statistic results are projected on a hypervoxel template. Finally, significant clusters of hypervoxels are identified. Figure from Luque Laguna (2019) [19].

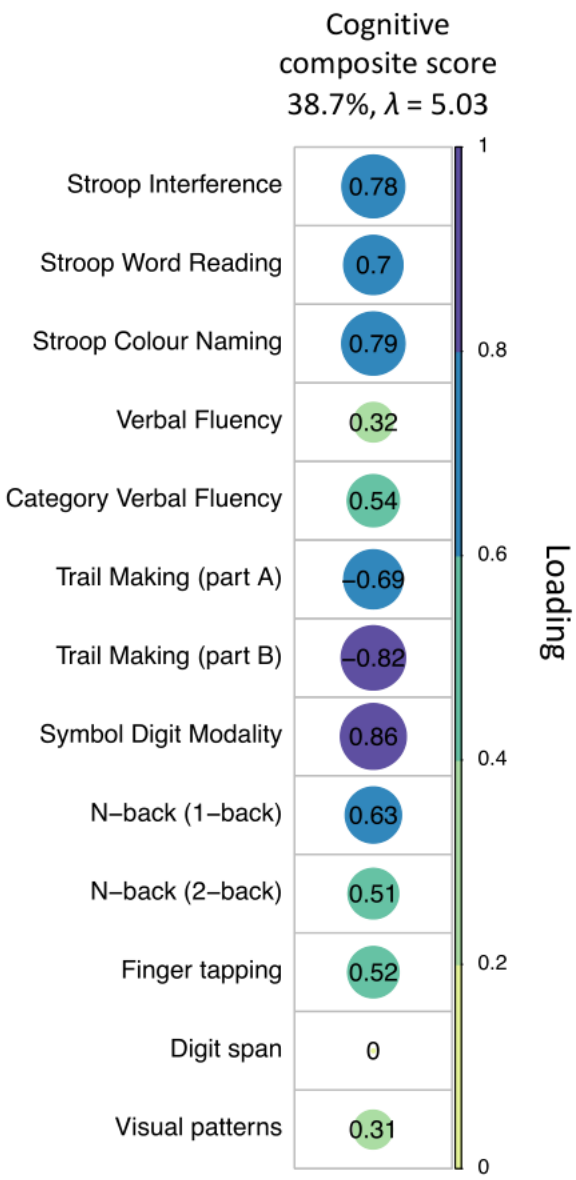

Figure 3. PCA of the cognitive data with varimax rotation.

Plot summarizing how each variable is accounted for in the extracted PC. The absolute correlation coefficient is plotted. Color intensity and the size of the circles are proportional to the loading. This PC accounted for 38.7% of the total variance and included measures from all test domains, except for the digit span. Four patients were excluded from the PCA because of missing data. The final sample size for the PCA was n=21 patients.

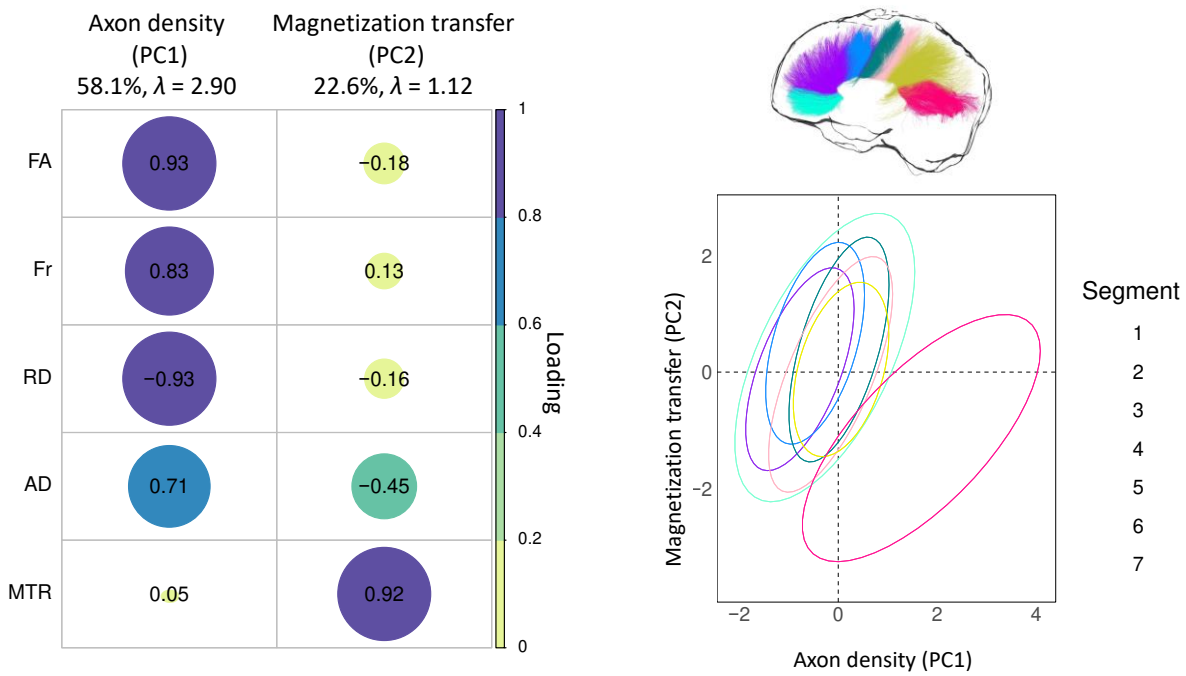

Figure 4. PCA of the microstructure metrics with varimax rotation.

Left: Plot summarizing how each variable is accounted for in every principal component. The absolute correlation coefficient is plotted. Color intensity and the size of the circles are proportional to the loading. The final sample size for the PCA was n=25 for the HD group and n=24 for the control group. Right: Segment clustering based on PC1 and PC2. The horizontal axis shows increasing restriction or hindrance perpendicular to the main axis of the bundles. The vertical axis represents an increase in MTR. Each point represents one subject. Concentration ellipsoids cover 95% confidence around the mean. Segment 7 appears to encompass most of the data variability.

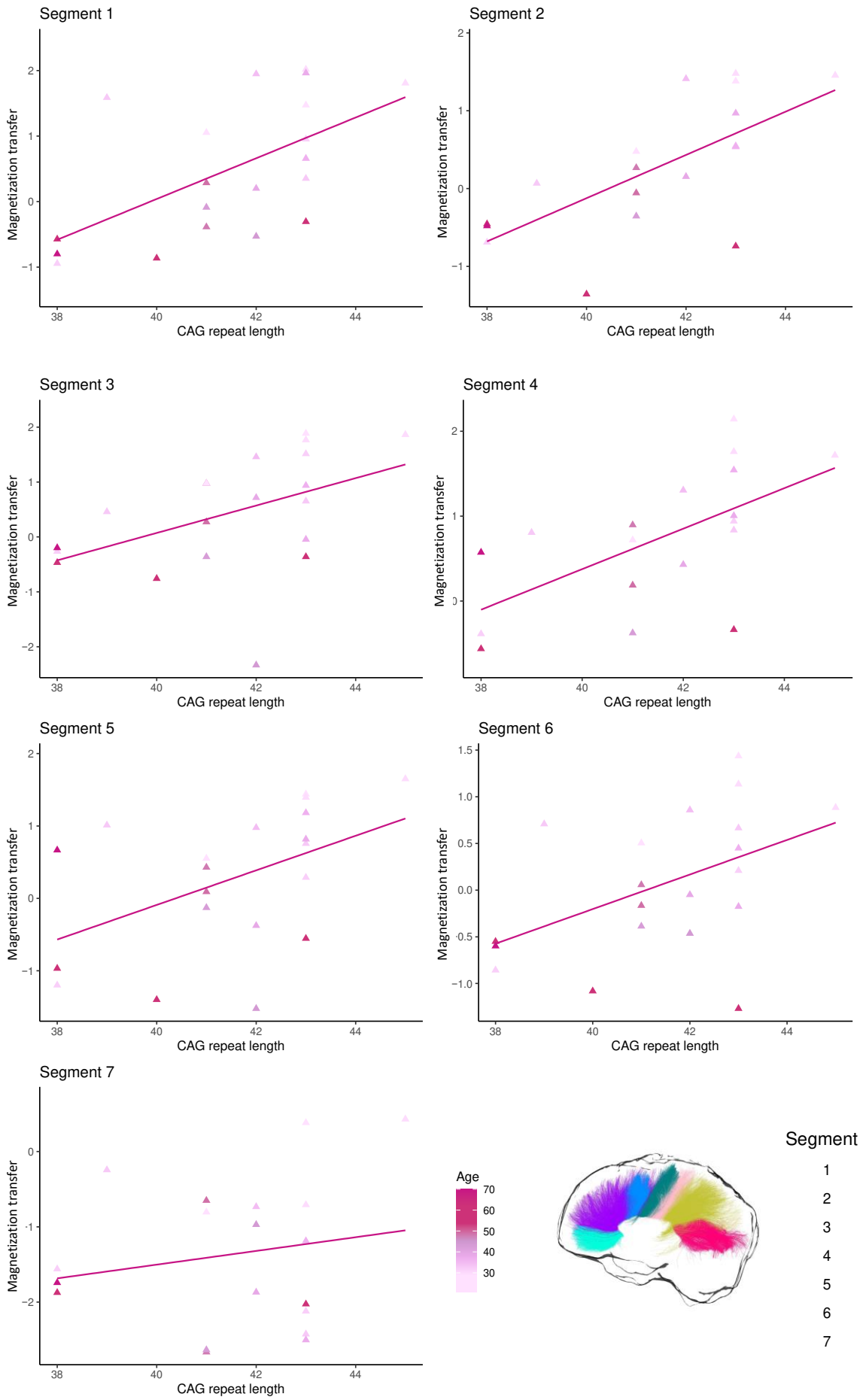
Segment 1
Segment 2
Segment 3
Segment 4
Segment 5
Segment 6
Segment 7
Magnetization transfer
CAG repeat length
Age
70
60
50
40
30
Segment
1
2
3
4
5
6
7

1132

1133 ***Figure 6. Relationship between magnetization transfer in each callosal segment and CAG repeat***
1134 ***length in patients.***

1135

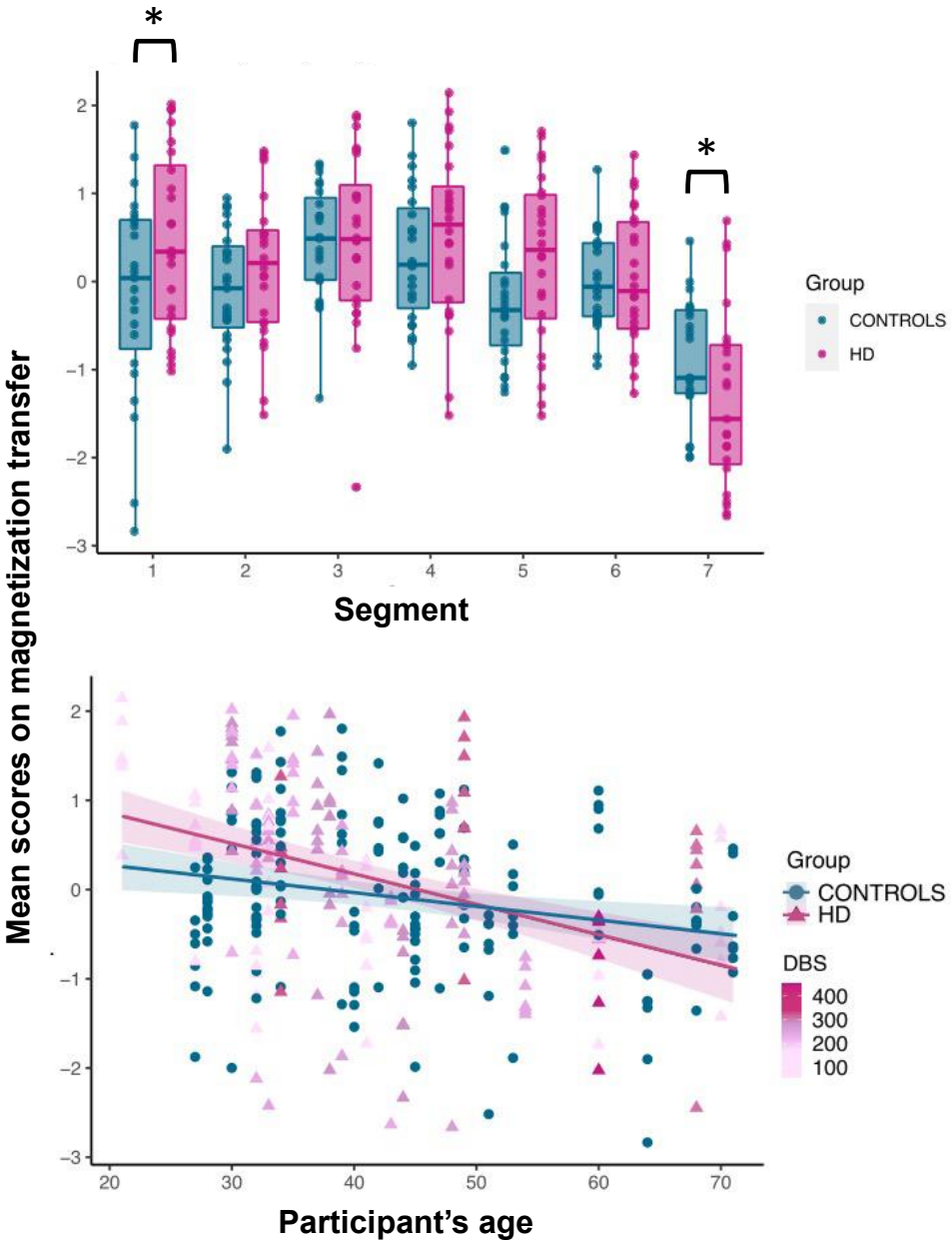

1136

1137 ***Figure 5. Callosal magnetization transfer: patient-control differences across callosal segments***
1138 ***(top), and relationship between age and inter-individual variability in the magnetization transfer***
1139 ***component (bottom).***

1140 *A group-by-segment interaction effect (p = 0.04) was observed for callosal magnetization transfer,*
1141 *indicating that the effect of group was different for different callosal segments. Patients presented*
1142 *significantly higher magnetization transfer compared to controls in segment 1 (p = 0.016), and*
1143 *significantly lower in segment 7 (p = 0.034). Overall, scores on the magnetization transfer component*
1144 *for the patient group were higher than controls in the more anterior portions of the CC but lower in*
1145 *posterior portions. Additionally, a significant interaction effect between group and age indicated that,*
1146 *while older HD patients presented significantly lower magnetization transfer than age-matched*

*controls, the opposite was true for younger HD patients. * p < 0.05, ** p < 0.01, *** p < 0.001, Bonferroni-corrected.*

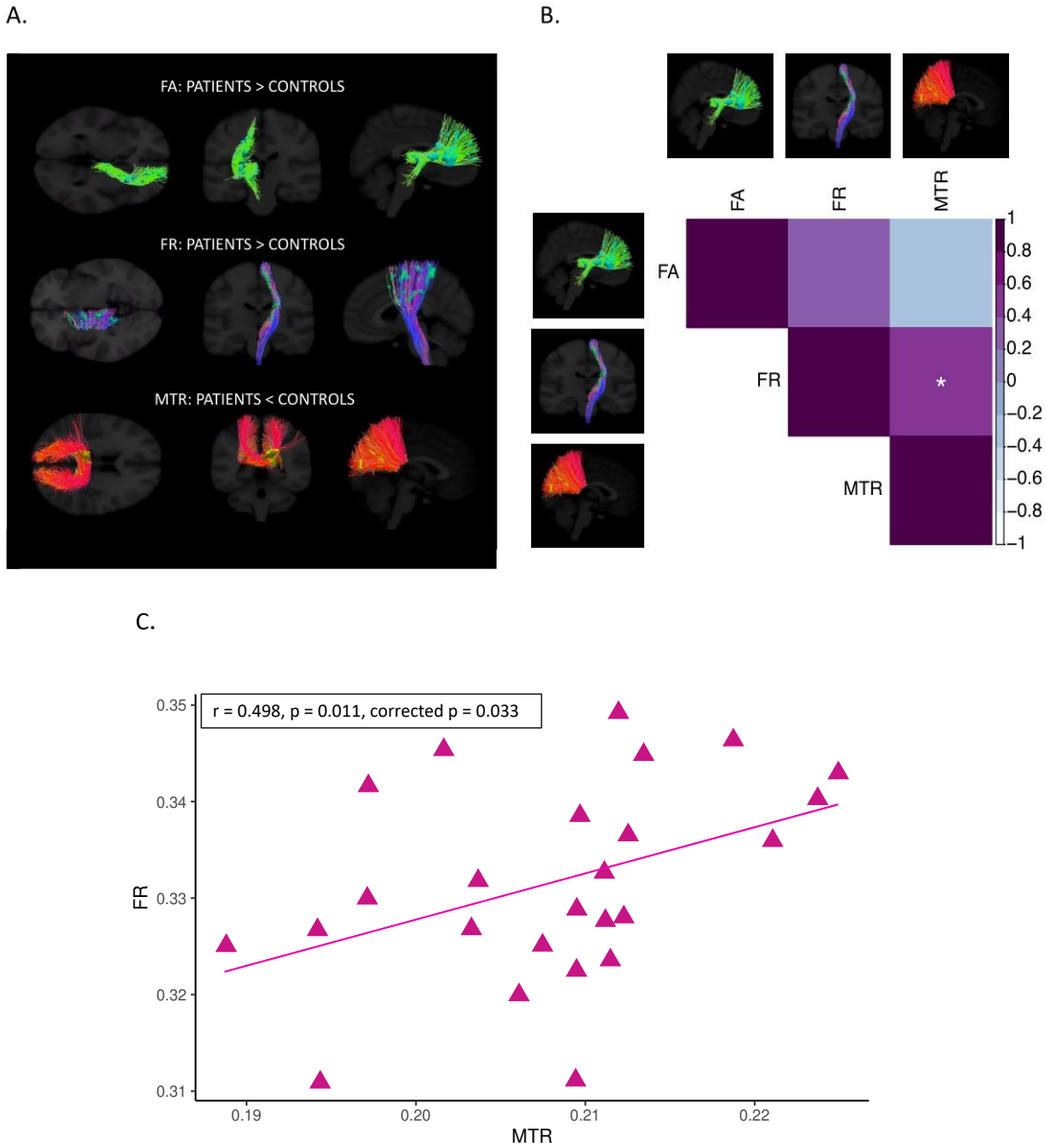

Figure 7. Results of the cluster-analysis obtained with TBCA between patients and controls (A), Spearman correlations between significant TBCA clusters in patients (B)[* p < 0.05, ** p < 0.01, *** p < 0.001, Bonferroni-corrected], and plot of MTR in the posterior callosum vs FR in the CST in patients (C).